

© Timothy P. Garvin

Report Documentation Page			Form Approved OMB No. 0704-0188		
Public reporting burden for the collection of information is estimated to average 1 hour per response, including the time for reviewing instructions, searching existing data sources, gathering and maintaining the data needed, and completing and reviewing the collection of information. Send comments regarding this burden estimate or any other aspect of this collection of information, including suggestions for reducing this burden, to Washington Headquarters Services, Directorate for Information Operations and Reports, 1215 Jefferson Davis Highway, Suite 1204, Arlington VA 22202-4302. Respondents should be aware that notwithstanding any other provision of law, no person shall be subject to a penalty for failing to comply with a collection of information if it does not display a currently valid OMB control number.					
1. REPORT DATE <b>2012</b>		2. REPORT TYPE		3. DATES COVERED <b>00-00-2012 to 00-00-2012</b>	
4. TITLE AND SUBTITLE <b>Fabrication, Characterization, and Wettability Analysis of a Microstructured Hybrid Hydrophobic/Hydrophilic Surface</b>			5a. CONTRACT NUMBER		
			5b. GRANT NUMBER		
			5c. PROGRAM ELEMENT NUMBER		
6. AUTHOR(S)			5d. PROJECT NUMBER		
			5e. TASK NUMBER		
			5f. WORK UNIT NUMBER		
7. PERFORMING ORGANIZATION NAME(S) AND ADDRESS(ES) <b>University of Illinois at Urbana-Champaign, Department of Mechanical Engineering, Urbana, IL, 61801</b>			8. PERFORMING ORGANIZATION REPORT NUMBER		
9. SPONSORING/MONITORING AGENCY NAME(S) AND ADDRESS(ES)			10. SPONSOR/MONITOR'S ACRONYM(S)		
			11. SPONSOR/MONITOR'S REPORT NUMBER(S)		
12. DISTRIBUTION/AVAILABILITY STATEMENT <b>Approved for public release; distribution unlimited</b>					
13. SUPPLEMENTARY NOTES					
14. ABSTRACT <b>This thesis explores the effects of surface chemistry and geometry on wettability of Hybrid Surfaces. The Hybrid Surfaces are composed of many micropillars with hydrophobic sidewalls and hydrophilic tops. The surfaces are designed with stable dropwise condensation in mind, which can increase heat fluxes by an order of magnitude over those of filmwise condensation. Based on the literature and technical constraints on fabrication, four Hybrid Surfaces are designed, fabricated characterized and tested for wettability. A model based on energy minimization is referenced and fits well to the experimental data. Experiments suggest a composite interface for droplets resting on the surface due to increasing advancing and receding angles with tower spacing. Future work is anticipated to include droplet nucleation and growth experiments, and quantification of the thermal performance during condensation.</b>					
15. SUBJECT TERMS					
16. SECURITY CLASSIFICATION OF:			17. LIMITATION OF ABSTRACT <b>Same as Report (SAR)</b>	18. NUMBER OF PAGES <b>79</b>	19a. NAME OF RESPONSIBLE PERSON
a. REPORT <b>unclassified</b>	b. ABSTRACT <b>unclassified</b>	c. THIS PAGE <b>unclassified</b>			

FABRICATION, CHARACTERIZATION, AND WETTABILITY ANALYSIS OF A  
MICROSTRUCTURED HYBRID HYDROPHOBIC/HYDROPHILIC SURFACE

BY

TIMOTHY P. GARVIN

THESIS

Submitted in partial fulfillment of the requirements  
for the degree of Master of Science in Mechanical Engineering  
in the Graduate College of the  
University of Illinois at Urbana-Champaign, 2012

Urbana, Illinois

Adviser:

Professor Anthony Jacobi

## ABSTRACT

This thesis explores the effects of surface chemistry and geometry on wettability of Hybrid Surfaces. The Hybrid Surfaces are composed of many micropillars with hydrophobic sidewalls and hydrophilic tops. The surfaces are designed with stable dropwise condensation in mind, which can increase heat fluxes by an order of magnitude over those of filmwise condensation. Based on the literature and technical constraints on fabrication, four Hybrid Surfaces are designed, fabricated, characterized and tested for wettability. A model based on energy minimization is referenced and fits well to the experimental data. Experiments suggest a composite interface for droplets resting on the surface due to increasing advancing and receding angles with tower spacing. Future work is anticipated to include droplet nucleation and growth experiments, and quantification of the thermal performance during condensation.

## ACKNOWLEDGEMENTS

First and foremost the author would like to thank the Army Corps of Engineers Engineer Research and Development Center Construction Engineering Research Laboratory and PI Dr. Charles Marsh for funding this research and ultimately this Master's project. Special thanks to adviser Dr. Anthony Jacobi and colleagues in the University of Illinois Urbana Champaign Air Conditioning and Refrigeration Center for their valuable support in preparation of this manuscript. The author also thanks Dr. Jorge Alvarado and his PhD student Chun-Wei Yao for their expertise and heat transfer experimentation of these surfaces. In addition, the help provided by Glennys Mensing, Michael Hansen, and the Micro-Nano Mechanical Systems Cleanroom staff with regards to micro-scale fabrication techniques is greatly appreciated. Finally, I would like to thank my fiancée and family for their support and encouragement.

## TABLE OF CONTENTS

<b>LIST OF SYMBOLS AND TERMINOLOGY .....</b>	<b>VI</b>
<b>CHAPTER 1: INTRODUCTION .....</b>	<b>1</b>
1.1 MOTIVATION .....	1
1.2 SCOPE OF THE RESEARCH .....	3
1.3 OVERVIEW.....	3
<b>CHAPTER 2: CONTACT ANGLE THEORY.....</b>	<b>5</b>
2.1 CONTACT ANGLE OF WETTED AND COMPOSITE INTERFACES .....	5
2.2 VARIABILITY DUE TO LOCAL FREE ENERGY MINIMA .....	7
2.3 FIGURES .....	10
<b>CHAPTER 3: HYBRID SURFACE DESIGN PARAMETERS .....</b>	<b>11</b>
3.1 MOTIVATION FOR HYBRID SURFACE STRUCTURE .....	11
3.2 DESIGN PARAMETERS FOR FABRICATED HYBRID SURFACES.....	14
3.3 FIGURES .....	16
<b>CHAPTER 4: HYBRID SURFACE FABRICATION .....</b>	<b>19</b>
4.1 FABRICATION OVERVIEW .....	19
4.2 PROCESS DIAGRAM .....	22
4.3 PROCESS DETAIL .....	24
4.4 FIGURES .....	36
<b>CHAPTER 5: CHARACTERIZATION .....</b>	<b>40</b>
5.1 PROFILOMETRY .....	40
5.2 SCANNING ELECTRON MICROSCOPY .....	41
5.3 ENERGY-DISPERSIVE X-RAY SPECTROSCOPY .....	41
5.4 TIME-OF-FLIGHT SECONDARY ION MASS SPECTROSCOPY.....	42

5.5 GONIOMETRY .....	43
5.6 FIGURES .....	46
<b>CHAPTER 6: RESULTS AND DISCUSSION.....</b>	<b>51</b>
6.1 FACTORS IN THE CONTACT ANGLE MODEL.....	51
6.2 ADVANCING ANGLE.....	54
6.3 RECEDING ANGLE .....	56
6.4 EQUILIBRIUM ANGLE .....	57
6.5 FIGURES .....	59
<b>CHAPTER 7: FUTURE WORK.....</b>	<b>61</b>
7.1 OBJECTIVES .....	61
7.2 DROPLET NUCLEATION .....	61
7.3 DROPWISE CONDENSATION HEAT TRANSFER .....	63
<b>REFERENCES .....</b>	<b>65</b>

## LIST OF SYMBOLS AND TERMINOLOGY

$\gamma^{SA}$  surface energy of solid-air interface

$\gamma^{LS}$  surface energy of liquid-solid interface

$\gamma^{LA}$  surface energy of liquid-air interface

$\theta_Y$  Young's contact angle (smooth wetted interface)

$r_w$  Wenzel roughness factor

$\theta_w$  Wenzel contact angle (wetted interface)

$\theta_{CB}$  Cassie-Baxter contact angle (composite interface)

$f_1$  area fraction of the solid-liquid interface

$f_2$  area fraction of the liquid-air interface

TCL three-phase contact line

$F^{rel}$  difference in free energy between two states

$\rho$  relative position of the three-phase contact line

$\phi$  observed (apparent) contact angle

IC integrated circuit

MEMS/NEMS micro/nano electro mechanical systems

RIE reactive ion etcher

BOE buffered oxide etchant

ICP-DRIE Inductively Coupled Plasma Deep Reactive Ion Etcher

HF hydrofluoric acid

SEM Scanning Electron Microscopy



EDX Energy-Dispersive X-Ray Spectroscopy

TOF-SIMS Time-of-Flight Secondary Ion Mass Spectrometry

$\theta_{le}$  effective intrinsic angle of the micropillar tops

$\theta_1$  Young's angle of hydrophilic material

$x_1$  area fraction of hydrophilic material

$\theta_2$  Young's angle of the hydrophobic material

$x_2$  area fraction of hydrophobic material

$h$  tower height

$\theta_{sw}$  effective intrinsic advancing angle of micropillar sidewalls

$\theta_{eq}$  equilibrium angle

$\theta_{adv}$  advancing angle

$\theta_{rec}$  receding angle

$\Delta G$  free energy barrier to nucleation

$r_e$  critical radius of a condensed water droplet

$J$  nucleation rate of droplets above the critical radius

$r$  droplet radius

$r_{max}$  maximum droplet diameter

$\Delta T$  Temperature difference between vapor and surface

$T$  Temperature

$\sigma$  surface tension

$\rho$  density of water

$h_{fg}$  specific latent heat of evaporation

$\lambda$  thermal conductivity of water

$\rho_v$  density of water vapor

$\gamma$  heat capacity ratio

$R_g$  specific gas constant

## CHAPTER 1: INTRODUCTION

The overall goal of this project is to design, fabricate, characterize, and test Hybrid Surfaces for their heat transfer capability. A Hybrid Surface is defined as a surface with an array of towers which are intrinsically hydrophilic (water attracting) on the tops of the towers and hydrophobic (water repelling) on the sidewalls. The purpose of this dichotomy of hydrophobic and hydrophilic surfaces is to promote and maintain dropwise condensation.

### 1.1 Motivation

In many condensing heat transfer applications, hydrophilic surfaces are used because they are stable to fouling and facilitate simple condensate management schemes. Strategies using hydrophilic surfaces in condensation rely on filmwise condensation, in which a film of water is maintained on the surface. Since conduction of heat through the water is necessary, the film incidentally creates a heat transfer resistance and causes a drop in heat flux compared that of dropwise condensation. Condensing surfaces that maintain dropwise condensation and promote water drainage could significantly enhance the thermal performance in condensing heat transfer applications. Through an outside energy source (typically gravity, but perhaps vibration could be used) droplets can roll off, revealing bare surface available for condensation. Since this latent heat transfer is continuously allowed to occur without a generating a thin film, a higher heat flux

is attainable to possibly more than 20x the heat flux of filmwise condensation [1]. Hydrophobic surfaces are typically good at removing moisture easily, allowing for dropwise condensation to occur. However, problems arise in industry when steady erosion of hydrophobic films requires the need for periodic recoating [2], or when the hydrophobic surface is simply so water repellant that it is relatively difficult to condense to compared to a hydrophilic surface. Hybrid Surfaces are intended to take the best benefits of both surfaces and use them where they are needed. Hydrophilic surface area is limited to the tops of the micropillars to maintain a source of easily condensable surface area. The hydrophobic sidewalls maintain droplet stability to keep the droplets on the tops of the pillars, which is one way to ease droplet shedding and reduce coating erosion. Through the combination of these surfaces, sustainable and stable dropwise condensation may be attainable.

The potential impact and significance of these surfaces is yet to be seen. If the surface is able to maintain dropwise condensation, it can be used to vastly improve efficiency in many thermal management systems. Possible use of these surfaces could be in reducing the size of condensers or cooling towers. These surfaces could also be used to improve humidity management.

## 1.2 Scope of the Research

The purpose of this research project is to design a variety of patterns for these Hybrid Surfaces, fabricate each of these designs, characterize the surface chemistry, and characterize its wettability. Patterns were designed with constraints provided by the resolution of the lithography process and with guidance from the literature. The fabrication process utilized a variety of IC and MEMS fabrication techniques to construct structures in the microscale range. A combination of SEM, EDX, and TOF-SIMS characterization processes allowed the identification of surface chemistry on specific parts of the surface (tower tops and sidewalls) to verify the hydrophobicity or hydrophilicity of each respective area. Finally, goniometry was used to characterize wettability. The experimental results from goniometry were compared to variations of the Cassie-Baxter and Wenzel models in order to predict the performance of designs not tested experimentally. This thesis encompasses the goals achieved in the first two out of three years in this research project. Future work consists of measuring condensation rate and water removal rate, which will emulate a real-world scenario should these surfaces be used in industry.

## 1.3 Overview

The thesis is broken up into 7 chapters which describe the process from design to testing. Chapter 2 summarizes a brief overview of wettability theory from the early 1800's to what is used in present research. Chapter 3 describes the design

parameters and constraints used in the fabrication of Hybrid Surfaces. Chapter 4 provides a detailed overview of the fabrication process. Chapter 5 outlines characterization methods and results. Chapter 6 compares wettability results to model predictions provided by Cassie-Baxter and Wenzel models. Finally, Chapter 7 describes the future of the project, where droplet growth mechanisms and droplet shedding will be tested.

## CHAPTER 2: CONTACT ANGLE THEORY

### 2.1 Contact angle of wetted and composite interfaces

The hydrophobicity or hydrophilicity of a surface can be described by finding its “contact angle,” which describes the shape of a droplet as it sits on a surface. Young first described the equilibrium shape of a droplet and its dependence on three interfacial surfaces: one between the liquid and the air, another between the liquid and the solid, and one between the solid and the air [3]. The cosine of the angle between the liquid and solid is a function of the Gibbs free energy of these interfaces, which leads to his discovery of the so-called Young’s equation

$$\gamma^{SA} - \gamma^{LS} = \gamma^{LA} \cos \theta_Y \quad (1)$$

where  $\gamma^{SA}$  is the surface energy of the solid and air interface,  $\gamma^{LS}$  is surface energy of the liquid and solid interface,  $\gamma^{LA}$  is surface energy of the liquid and air interface, and  $\theta_Y$  is the contact angle (Young’s angle or intrinsic contact angle). Contact angles less than 90 degrees are considered “hydrophilic,” a general attraction to water. Contact angles greater than 90 degrees exhibit “hydrophobic” behavior, a general repulsion to water. Figure 1 shows how a hydrophobic droplet may interact with a surface.

To build further on this concept, the roughness features of the solid-liquid interface were investigated by Wenzel. With a roughness factor  $r_w$  described as the actual amount of surface area over the superficial or “geometric” surface, he described the contact angle is a function of roughness with the equation [4]

$$r_w \cdot (\gamma^{SA} - \gamma^{LS}) = \gamma^{LA} \cos \theta_w \quad (2)$$

Therefore, the Young’s angle was heretofore described as the contact angle of a surface that is perfectly smooth ( $r_w = 1$ ), versus the Wenzel angle  $\theta_w$  when roughness is a factor ( $r_w > 1$ ).

Furthermore, a droplet on a rough surface with tall enough asperities may exhibit what is called a composite interface. These droplets maintain contact with the tops of asperities, while at the same time many air pockets may be trapped underneath the droplet, creating a “composite” interface. The Cassie-Baxter model describes this type of interface through the equation [5]

$$\cos \theta_{CB} = f_1 \cos \theta_Y - f_2 \quad (3)$$

Where  $\theta_{CB}$  is the apparent Cassie-Baxter contact angle (the contact angle if it were measured in this equilibrium state),  $f_1$  is the area fraction of the solid-liquid interface, and  $f_2$  is the area fraction of the liquid-air interface. Diagrams of the



“Wenzel” (wetted) and “Cassie-Baxter” (composite) equilibrium states are shown below in Figure 2.

## 2.2 Variability due to local free energy minima

The Wenzel and Cassie-Baxter models are generalized equations to describe the minimum equilibrium energy state of a droplet on a surface. In real conditions, the absolute minimum-energy equilibrium state is not necessarily the state at which droplets will always settle. The three-phase contact line (TCL), or the edge of the droplet touching the surface and the surrounding air, may settle in a local equilibrium state which would ultimately change the shape of the droplet. As the TCL is about to advance across the surface, the droplet exhibits a relatively higher contact angle called the advancing angle. When the TCL is about to retract across the surface, the contact angle may drop to a relatively low value, called the receding angle. Slight variations of these definitions are often adopted in the literature. The difference between the advancing angle and the receding angle is what is known as contact angle hysteresis. The concept of contact angle hysteresis was mentioned by Cassie and Baxter but the first reasonable approach to understanding this phenomenon was developed by Shuttleworth and Bailey [6]. They described contact angle hysteresis as the result of the existence of many equilibrium states due to the inevitable structure of roughness on all surfaces. As the droplet advances across the surface, enough energy is put behind the TCL to push the droplet to a higher energy and settling in a higher local equilibrium state,

called a “metastable” state. As the TCL recedes across the surface, another local high energy state can be reached where the contact angle is relatively lower. To reach these local metastable states, a large amount of energy called a “free energy barrier” has to be overcome to allow the TCL to settle into these states [7, 8]. This energy was described by Good [9] as a “contortion energy” which the TCL has to overcome. As the roughness decreases, the TCL has to “contort” less and therefore contact angle hysteresis decreases [9].

Later, Johnson and Dettre referenced this concept of multiple equilibrium states from Shuttleworth and Bailey, and free energy barriers from Good, to develop a computational model describing contact angle hysteresis [10]. The model offered insight as to how extensive free energy barriers were under certain situations, whether the surface is wetted or in a composite state. Between any two positions of the TCL, the relative free energy between each state can be determined by the equation

$$F^{rel} = \frac{2\pi\rho^2}{1+\cos\varphi} - \pi r_W \rho^2 \cos\theta_Y \quad (4)$$

Where  $F^{rel}$  is the difference in free energy between the two states (units in  $\text{cm}^2$ , considered an effective area),  $\rho$  is the x-position of the three-phase contact line, and  $\varphi$  is the observed (apparent) contact angle. The amount of free energy in a droplet is dependent on the intrinsic angle of the solid surface and the type of

equilibrium state into which the droplet settles. Through this model they found that composite droplets will be less dependent on the degree of roughness, since the amount of contact between the solid-liquid interface is reduced. As a result, the free energy barriers to TCL movement are reduced. As the barriers are reduced, contact angle hysteresis will decrease since it is easier to move the TCL in either direction. Therefore, composite surfaces will exhibit less contact angle hysteresis than wetted surfaces. They went on to verify their model with experimental data [11]. Due to this contact angle hysteresis behavior, it is difficult to determine the hydrophobicity or hydrophilicity of a surface with only one sessile drop contact angle measurement. In order to have a complete understanding of surface behavior, both advancing and receding angles should be reported [12]. In addition to having a range of contact angles for a droplet to manifest on a surface, the contact angle hysteresis also provides a metric for how easily a droplet can “roll off” a surface. In general, if contact angle hysteresis is low, the droplet will be easier to remove from the surface.

## 2.3 Figures

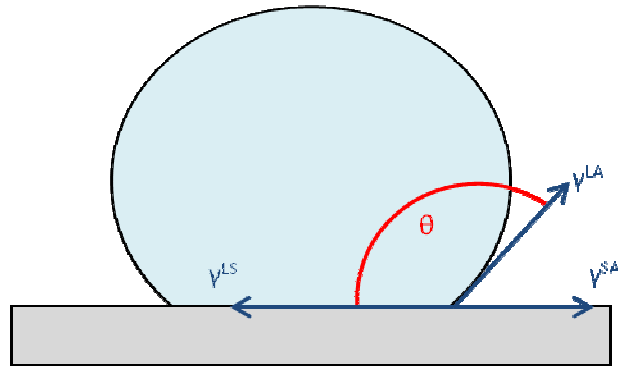


Figure 1: Contact angle of a water droplet

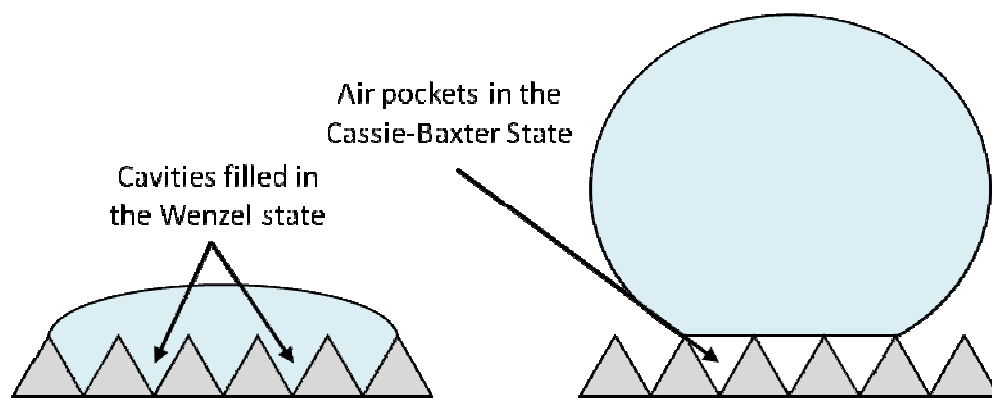


Figure 2: Wetted and composite interfaces

## CHAPTER 3: HYBRID SURFACE DESIGN PARAMETERS

### 3.1 Motivation for Hybrid Surface Structure

The motivation for the design of many hydrophobic surfaces for heat transfer purposes comes from the structure of the lotus leaf. The lotus plant has natural ability for water repellency and self-cleaning. As shown by Barthlott and Neinhuis, a combination of low-surface energy materials (lotus leaves containing epicuticular wax crystalloids) along with its surface roughness work together to form a superhydrophobic surface. This effect was therefore named the “lotus-effect” [13].

In contrast to the highly hydrophobic lotus leaf, a Hybrid Surface must have unique characteristics to achieve not only rapid shedding of droplets but also rapid droplet nucleation. Hybrid Surfaces consist of square pillars which maintain a hydrophilic material on the pillar tops and hydrophobic material on the tower sidewalls (Figure 3). Varanasi *et al.* were the first to coin the term “Hybrid Surface,” due to their experiments with similarly structured surfaces [14, 15]. They found that they could spatially control the nucleation of water on hydrophilic strips between hydrophobic strips and hydrophilic areas on the top of hydrophobic towers. The structure and surface chemistry of the Hybrid Surface is described further in this chapter.

The hydrophobic material must, by definition, have an intrinsic contact angle greater than 90 degrees. Preferably, the contact angle should be very large in order to create an effective surface for water repellency. A very common material to use is Fluorine or rather any molecule which contains a large amount of Fluorine groups [16, 17]. Any Teflon-like material will help maintain a surface which will, at a minimum, show a contact angle of about 112 degrees. A plasma deposition of a polymer like  $(C_2F_4)_n$  is used in this study, providing an adequate low-surface energy coating.

For a hydrophilic material, a thermally grown silicon oxide ( $SiO_2$ ) is a convenient material when it comes to fabricating microstructures. Most Integrated Circuit (IC) and Micro/Nano Electro Mechanical Systems (MEMS/NEMS) fabrication depend on the use of silicon wafers to achieve small scale structures. The contact angle of  $SiO_2$  is consistently below 90 degrees but may change from 0-50 degrees depending on environmental conditions and cleanliness of the surface [18]. For a Hybrid Surface, the contact angle of  $SiO_2$  is adequate.

One goal of a Hybrid Surface is to maintain Cassie-Baxter state stability in droplets. Air pockets must form in the pockets between the micropillars. Design criterion for Cassie-Baxter state stability was described by Patankar in 2003. Essentially, the pillar width should be very slender compared to pillar height [19]. This design will allow the Cassie-Baxter state to have an overall lower energy

state and therefore be the most favorable state for the droplet. In addition, there is a transitional range from Cassie-Baxter to Wenzel state stability around a critical point dependent on pillar width and pillar pitch (spacing). In order to maintain Cassie-Baxter state stability as the most favorable energy state, the ratio of pillar width to pitch should be lower than this critical value.

Ideally, a Hybrid Surface should remove moisture easily. This is a requirement that deals specifically with contact angle hysteresis. As mentioned earlier, generally, droplet roll off is easier for surfaces with low contact angle hysteresis. For surfaces with asperities (such as Hybrid Surface pillars), a low contact angle hysteresis may be caused by the surface structure. On one hand, hysteresis may be low because a microstructure of tall, slender pillars will help improve droplet rolloff, since the composite interface is maintained [20]. On the other hand, the droplet TCL may remain “pinned” to the edges of the asperities. For example, as a droplet advances across a surface, the droplet may be pinned before it crosses the gap to the next tower (Figure 4). For a receding case, the same may happen (Figure 5). If the TCL does not move easily in either direction, hysteresis will occur. This pinning occurs frequently for sawtooth grooves, less frequently for an array of rectangular or pyramidal asperities, and least likely for an array of hemispherical, or cylindrical asperities [21]. From a modeling standpoint, rectangular asperities are the easiest to model (since they can be analyzed from a 2-D standpoint like the Cassie-Baxter or Wenzel equations). From a MEMS/IC

fabrication standpoint, flat tops and straight sidewalls are the easiest to fabricate, as explained in a later chapter. Therefore, the Hybrid Surfaces described herein contained an array of tall, slender, moderately spaced rectangular asperities. The main parameter to change was the space between towers, since this value has a dramatic effect on both contact angle hysteresis and the Cassie-Baxter state stability.

### 3.2 Design parameters for fabricated Hybrid Surfaces

The design of each Hybrid Surface, as explained earlier, remained constant with the exception of changing the space between each tower. On a 4-inch silicon wafer, 4 30 mm x 30 mm samples can be fabricated. Therefore, 4 designs were fabricated and tested. Refer to Figure 6 and Table 1 for dimensions and values for each design. The micropillar width dimension (a) remained constant at 25  $\mu\text{m}$ . This dimension was constrained by the degree of accuracy attainable with the lithography technique available at the Micro-Nano Mechanical Systems Cleanroom (MNMS). The mask aligner uses a proximity (shadow) printing solution, which allows 50  $\mu\text{m}$  of space between mask and wafer, with 405 nm light, and a resist thickness of about 5  $\mu\text{m}$ . The minimum resolution given by this setup is given by the equation [22]

$$R = \frac{3}{2} \sqrt{\lambda \cdot \left(s + \frac{z}{2}\right)} = \frac{3}{2} \sqrt{0.405 \cdot \left(50 + \frac{5}{2}\right)} = 6.9 \mu\text{m} \quad (5)$$



It was desired that the tower widths are reasonably higher than this resolution limit to reduce the rounding of corners. In addition, the space between towers should be higher than this value to prevent the merging of towers. In order to get a reasonable range of values that will change the contact angle a noticeable amount, the space between each tower was determined to be, for each design, 0.5x, 1x, 1.5x and 2x the tower width. Therefore, with all of these constraints in mind, the chosen values for space between towers (b) were 12.5  $\mu\text{m}$ , 25  $\mu\text{m}$ , 37.5  $\mu\text{m}$ , and 50  $\mu\text{m}$ . In many prior reports in the literature, the value of center-to-center spacing is reported (sometimes called pitch, p) and is also given in Table 1.

### 3.3 Figures

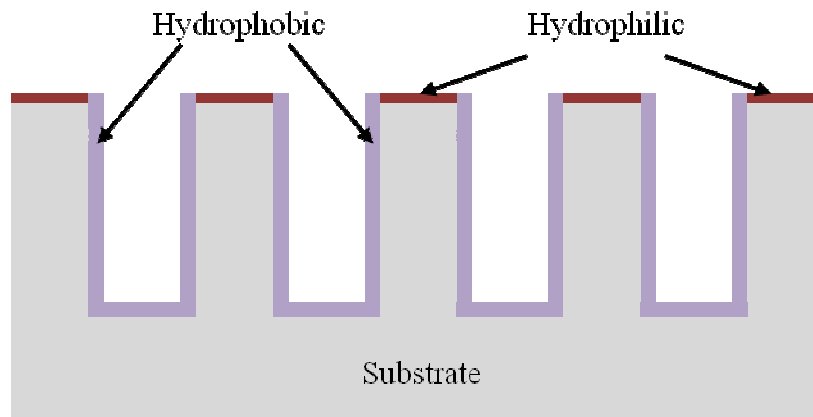


Figure 3: Structure of a Hybrid Surface

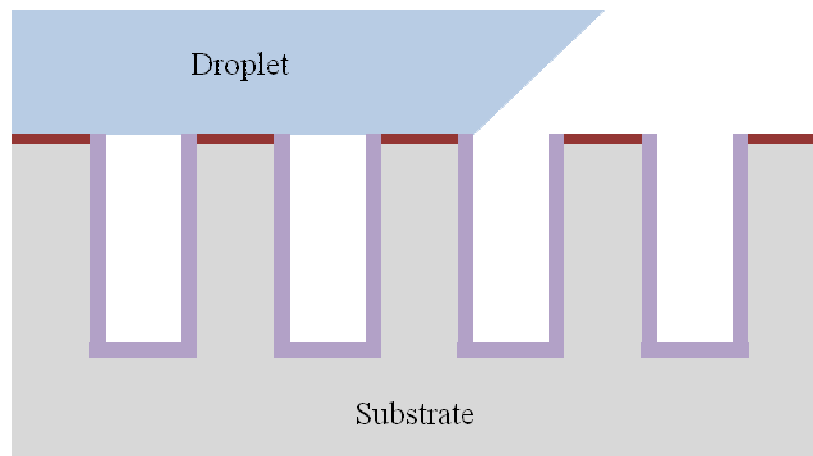


Figure 4: “Pinning” in an advancing case

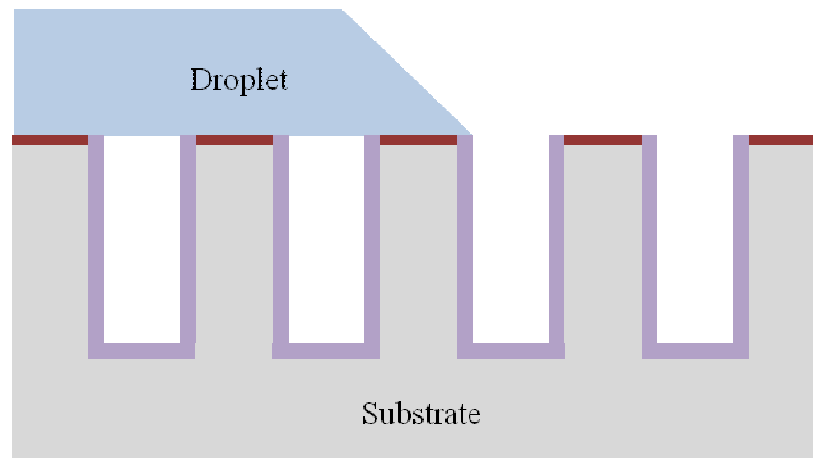


Figure 5: "Pinning" in a receding case

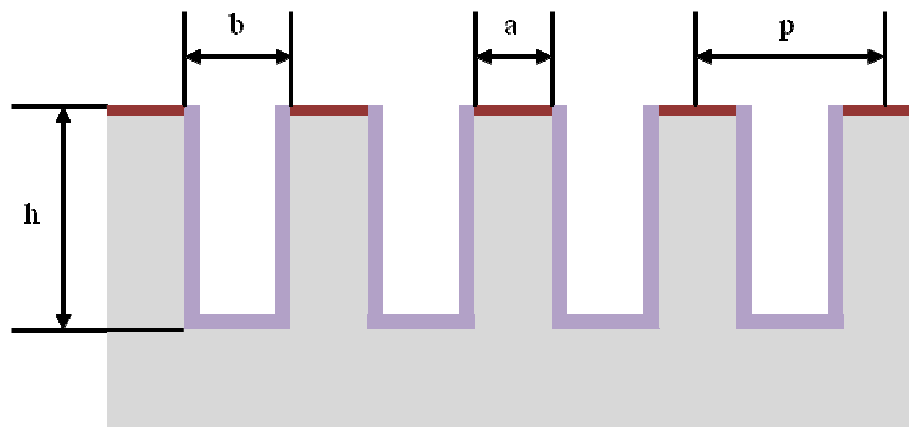


Figure 6: Critical dimensions

Table 1: Critical dimensions of 4 Hybrid Surface designs

Design	Width (a)	Spacing (b)	Pitch (p)	Height (h)
1	25 $\mu\text{m}$	12.5 $\mu\text{m}$	37.5 $\mu\text{m}$	75 $\mu\text{m}$
2	25 $\mu\text{m}$	25 $\mu\text{m}$	50 $\mu\text{m}$	75 $\mu\text{m}$
3	25 $\mu\text{m}$	37.5 $\mu\text{m}$	67.5 $\mu\text{m}$	75 $\mu\text{m}$
4	25 $\mu\text{m}$	50 $\mu\text{m}$	75 $\mu\text{m}$	75 $\mu\text{m}$

## CHAPTER 4: HYBRID SURFACE FABRICATION

### 4.1 Fabrication Overview

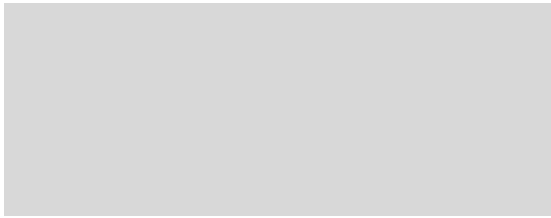
A Hybrid Surface can be made using a variety of MEMS and IC fabrication techniques. Shown below is a summary of the steps (a “recipe”) required to develop a Hybrid Surface from scratch. Later in this chapter, each step is described in more detail. A process diagram outlining each step is shown in section 4.2.

1. A 4-inch SSP (single-side polished) <100> silicon wafer was rinsed with Acetone, Isopropyl Alcohol (IPA), DI Water, IPA again, and dried with Nitrogen gas ( $N_2$ ).
2. Silicon wafer was placed (polished side up) in the March Reactive Ion Etcher (RIE) and exposed to Oxygen plasma, 100 W power for 1 minute.
3. Wafer was loaded in an oxidation tube furnace at 1100°C for 4 hours, 4 minutes. This procedure grows approximately 250 nm of  $SiO_2$ .
4. Repeated steps 1-2 on the polished side of the wafer to make sure no particles or organics remained.
5. Wafer was prebaked on hotplate (polished side up) at 110°C for 1 minute with a protective aluminum ring underneath it.
6. Spun 500  $\mu$ L of AP8000 (Adhesion Promoter) onto the polished side of the wafer. Spun at 3000 RPM for 30 seconds.

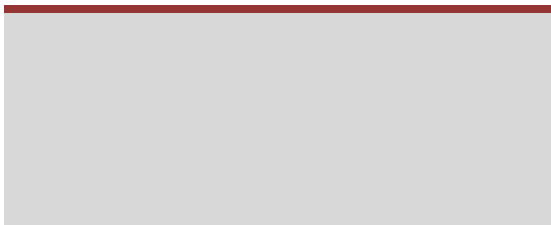
7. Spun 3000  $\mu\text{L}$  of SPR-220 Photoresist onto the polished side of the wafer.  
Spun at 3000 RPM for 30 seconds.
8. Placed wafer on a hot plate (with aluminum ring) at  $60^{\circ}\text{C}$  for 2 minutes.
9. Placed wafer on a hot plate (with aluminum ring) at  $110^{\circ}\text{C}$  for 1 minute.
10. Cooled wafer on an aluminum puck for 1 minute.
11. Flipped the wafer over to expose the unpolished side, repeated steps 5 through 10 to spin photoresist on this side.
12. Aligned the polished side of the wafer to the design mask (Figure 7, sample design shown in Figure 8), exposed the photoresist to 405 nm wavelength (H-Line) UV light, at a power of  $21.2 \text{ mW/cm}^2$  for 12 seconds (resulting exposure =  $254.4 \text{ mJ/cm}^2$ )
13. Mixed 4:1 ratio of DI water and AZ 400K developer (100 mL DI water, 25 mL of AZ 400K). With a dropper, developed only the alignment marks with this solution (Figure 9).
14. Aligned the unpolished side of the wafer to the window mask (Figure 10).  
Exposed the unpolished side with the same recipe as step 10.
15. Placed the entire wafer in the 4:1 DI water and AZ 400K solution.  
Developed for 1 minute with the polished side down, then turned over and developed for 1 more minute polished side up. Submerged the wafer in a DI water bath for 2 minutes. Inspected the wafer to ensure the pattern transferred.

16. Hard baked the resist on a hotplate at 110°C for 5 minutes, polished side up with the aluminum ring.
17. Prepared Buffered Oxide Etchant (BOE) in a PTFE container. Placed the wafer polished side up into the BOE solution for 2 minutes and 30 seconds. Submerged the wafer in a DI water bath for 1 minute 30 seconds.
18. Loaded the wafer (polished side up) into the Plasmatherm Inductively Coupled Plasma Deep Reactive Ion Etcher (ICP-DRIE). Etched the wafer using the Bosch Process. Length of etch time dependent is on mask design.
19. Once the etch finished,  $C_4F_8$  plasma was run for 1 minute to deposit 70 nm of Teflon-like material.
20. Flipped the wafer over to the unpolished side and loaded it into the STS ICP-DRIE. Ran a faster Bosch Process to etch approximately 85% the thickness of the wafer.
21. Placed the wafer, polished side up, into AZ 400T photoresist stripper for 24 hours at room temperature.
22. Cleaved the wafer around the edges that were etched on the unpolished side of the wafer. Placed in Gel-Pak Gel-Boxes (retention level X4) for storage and shipping.

## 4.2 Process Diagram



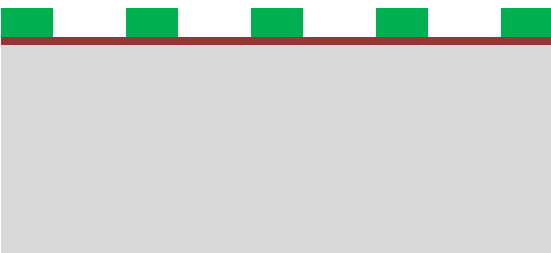
Step 1 – Clean with Acetone,  
IPA, DI, IPA, N<sub>2</sub> dry.  
Step 2- Oxygen plasma clean with  
March RIE



Step 3 – Oxidize wafer, grow 250  
nm of SiO<sub>2</sub>  
Step 4 – Clean again as in step 1  
and 2

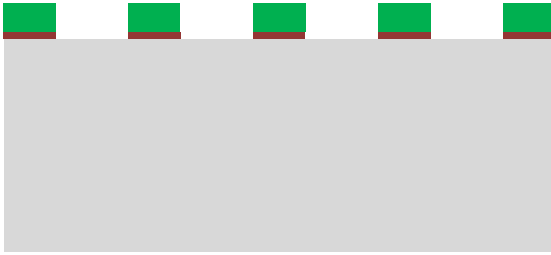


Steps 5-10 – Spin coat AP8000,  
SPR220 photoresist  
Step 11-12 (not shown) spin coat  
unpolished side

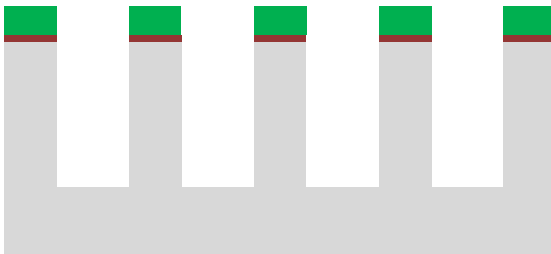


Steps 12-15, expose resist to H-  
Line UV light through the design  
mask, develop with AZ 400K  
Step 16 – hard bake

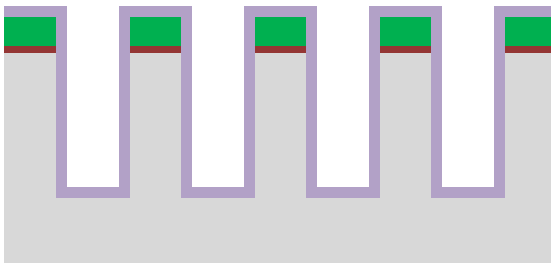




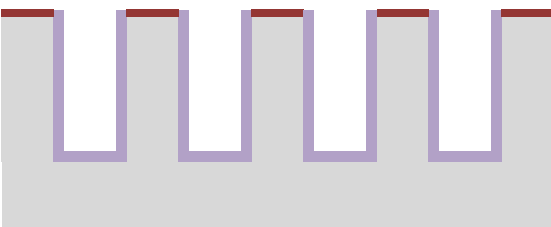
Step 17 – BOE etch away oxide to leave behind SiO<sub>2</sub> squares underneath photoresist



Step 18 – ICP-DRIE etch down 75  $\mu$ m to leave behind towers



Step 19 – Deposit 70 nm of Teflon-like hydrophobic coating  
Step 20 (not shown) - 85% etch on the backside



Step 21 – Dip wafer in AZ 400T for 24 hours, liftoff Teflon on top of resist to expose SiO<sub>2</sub> tops  
Step 22 – separate samples

### 4.3 Process Detail

In this section specific details of the fabrication process are discussed. A quick overview of this process is outlined in sections 4.1 and 4.2.

A 4-inch single side polished (SSP) <100> crystal structure wafer was used as the base substrate material. Silicon has many advantages for its use in a heat transfer surface, including its high thermal conductivity and its low coefficient of thermal expansion. Only one side was polished for the purpose of keeping costs down and since microscale features are only required on one side. Acetone and isopropyl alcohol (IPA) were used to clean off light organics. The acetone was washed away with IPA while it was still wet to avoid residue growth on the wafer. DI water washed away any dust particles on the surface, and IPA was used to rinse the wafer again since it dries without residue. An N<sub>2</sub> gun was used to dry the wafer such that no other products (such as water vapor in air) were blown onto the wafer.

The polished side of the wafer was placed face up into a March Reactive Ion Etcher (RIE). The chamber was pulled to vacuum, after which then 1 SCCM of Argon and 2 SCCM of Oxygen flowed into the chamber. The RIE was turned on for one minute at a power of 100W to remove any other organics that may have been stuck to the surface. The wafer was not flipped to clean the opposite

(unpolished) side. The polished side cannot touch the platen of the RIE, as it may cause scratches.

An oxidation tube furnace was preheated to 1100°C and wafer was loaded into it. 8 SCCM of oxygen flowed into the system, and the wafer was kept at this temperature for 4 hours, 4 minutes. The temperature and time amount are dependent on the Deal-Grove dry oxidation growth model [23]. Approximately 250 nm of silicon dioxide ( $\text{SiO}_2$ ) was grown on the wafer. Thermal oxide was grown onto the wafer initially to guarantee that a sufficient amount of hydrophilic material resided on the surface.

After the wafer was cleaned again after oxidation, the wafer was ready to undergo the photolithography process. In order to remove any excess moisture on the surface, the wafer was prebaked on a hotplate at 110°C for 1 minute. A clean protective aluminum ring was placed between the wafer and the hotplate to minimize contact with the hotplate surface. Following the prebake, the wafer was placed (polished side up) onto the vacuum chuck of the spinner. 500  $\mu\text{L}$  of adhesion promoter AP8000 was spun onto the polished surface at 3000 RPM for 30 seconds. The adhesion promoter was used to make the wafer more hydrophobic, such that water films would not form between the wafer and the resist and reduce adhesion. After adhesion promoter was spun on, 3000  $\mu\text{L}$  of positive photoresist SPR-220 was spun onto the wafer at 3000 RPM for 30

seconds. The resulting thickness of the resist ranged from 5-6  $\mu\text{m}$ . The resulting spin coat of photoresist will still contain an excess amount of solvent which keeps the resist fluid in storage. A soft bake was required before exposure to prevent the surface from adhering to the photomask while it was aligned in the mask aligner. With the protective aluminum ring, the wafer was placed on a 60°C hotplate for 2 minutes and a 110°C hotplate for 1 minute (such that the heat flux was gradual and not too intense to harm the resist). The wafer was then cooled on an aluminum puck for 1 minute before the unpolished side was spin coated. The polished side was coated first to avoid any contact with the polished silicon oxide surface and the vacuum chuck. The photoresist could touch the vacuum chuck since it was a sacrificial layer. Once the unpolished side had a spun coat film of AP8000 and SPR-220, the wafer was softbaked (with the aluminum ring) again, this time polished side down. The softbake heat treatment time remained the same (2 minutes at 60°C, 1 minute at 110°C, 1 minute cool). Due to the order of this process, the polished side of the wafer was exposed to more heat than the unpolished side. To remedy this problem, the wafer was turned over once more and softbaked again. As a result, both sides should have been hardened enough to expose in a mask aligner, but not too much such that no pattern can develop.

SPR-220 photoresist was chosen for its compatibility with chemical etching processes and plasma etching processes. It is a positive photoresist, which means that any exposure to UV light will make the resist undergo scission, or the

breaking of chemical bonds within the resist. Once these bonds are broken, the resist becomes soluble to AZ 400K photoresist developer. Locations that are not exposed to UV light will remain insoluble to AZ 400K and stay on the substrate.

The idea behind photolithography is to selectively expose parts of the photoresist to UV light, such that it dissolves away resist that is not desired in the final pattern. A figure demonstrating this concept is shown in Figure 11. Once the photoresist is spun on and soft baked, a photomask is placed over the resist. A photomask contains a chrome-printed design, such that it will either let light through or create a shadow. Any light that passes through will expose the resist. Therefore, a 1:1 pattern transfer occurs. Once scissioning occurs within the exposed resist, developer dissolves it away, leaving behind the unexposed material which composes of the desired pattern.

For the main design of the Hybrid Surfaces, the photoresist had to be patterned in such a way that many photoresist squares of equal size and equal spacing were arranged on the substrate. A photomask design was drawn in Auto-CAD 2012 and the 5-inch chrome mask was printed on soda-lime glass by Fineline Imaging. An example of a photomask design is shown in Figure 7. The mask was placed on top of the resist with the help of a mask aligner (Electronic Visions EV420 Double-Sided Aligner) which also contains the light source. An efficient exposure wavelength for SPR-220 is 405 nm, also known as h-line. To allow the correct

amount of exposure, approximately  $254 \text{ mJ/cm}^2$  of light energy must be used. The light typically has a power of  $21.2 \text{ mW/cm}^2$ , which prescribes a 12-second exposure time.

This process required double-sided lithography, which requires two photomasks and alignment between the two designs. The design mask exposed the polished side to the main design, composing of an array of many microscopic squares (Figure 8). The purpose of the design mask was to designate the main shape of the micropillars of the Hybrid Surface. The unpolished side was exposed to the window mask, which contains only a few lines which constitute the borders of each individual Hybrid Surface (Figure 10). The purpose of the design on the unpolished side was to make pathways to etch the silicon around the Hybrid Surfaces, such that the material would be thin enough to break and separate the samples. In order to ensure the front and back designs were aligned, fiducial (alignment) marks were incorporated into the mask (Figure 9). These circular target-like features were first formed on the polished side of the wafer, exposed alongside the main Hybrid Surface design. Before the wafer was flipped over to be exposed with the window mask, the fiducial marks were selectively developed with a dropper. The whole wafer was not dipped into the developer yet since the unpolished side had not been exposed. The window mask was loaded into the mask aligner, and the positions of the alignment marks on the mask were recorded in the computer. When the wafer was turned over to expose the other side, the

wafer was moved into a position where the already-developed alignment marks were aligned to the recorded values in the computer. Therefore, the mask remained accurately aligned with the design on the polished side, and completed Hybrid Surfaces could be separated without defects. Exposure time for the window mask is equivalent to the design mask exposure time (12 seconds).

The next step in photolithography is developing. The wafer was submerged in a previously prepared mixture of 4 parts DI water, 1 part AZ 400K developer. This mixture dissolves away any resist that has been exposed by UV light. In order to ensure the transport of solvent to both sides, the wafer was propped up slightly by a pair of wafer handling tweezers. In addition, the wafer was flipped after 1 minute, which disturbed the surface enough to dissolve away the rest of the exposed photoresist. After 2 total minutes of developing, the wafer was submerged in a DI water bath for 2 minutes. It is advised against leaving it in DI water for too long, as the photoresist may lose its adherence to the oxide layer.

Before any further steps were taken, the polished side of the wafer was inspected with an optical microscope. This inspection was to ensure that the pattern transferred correctly, that the developing step was complete (no more excess exposed resist), and that there were minimal defects in the design. Occasional defects, such as the merging of one or more squares, may occur due to dust particles landing between the photomask and the resist. There was no guarantee

that the surface would have a perfect pattern transfer, but one or two of these defects was tolerable, since the total amount of photoresist squares range from 160,000 to 640,000, depending on design.

Once the wafer was inspected for defects, and was deemed acceptable, the wafer was placed on a hotplate with aluminum ring once again. The temperature of the hotplate was 110°C and the wafer underwent a “hard bake” for 5 minutes. Since the remaining pattern no longer had to undergo any chemical changes, the remaining solvent within the resist could be baked out. The hard bake allowed the resist to adhere better to the substrate in preparation for the following fabrication steps. The polished side was kept face up during the hard bake, since special care must be taken to ensure the design is not spoiled.

The next step was to remove all silicon oxide that was not covered by photoresist. The silicon oxide was too thick to be plasma etched with a DRIE, and therefore had to be removed before the silicon underneath could be etched. A diluted hydrofluoric acid (HF) solution called buffered oxide etchant (BOE) was prepared in a PTFE container. For necessary precautions, a face shield, acid-resistant apron, and black acid gloves were worn during this process. The wafer was submerged in the BOE for 2 minutes and 30 seconds, as the etch rate was approximately 100 nm/minute. After the oxide etch the wafer was immediately placed in a running DI water bath for 1 minute 30 seconds. Again, since the



photoresist will lose its adherence in the presence of water, its time spent in a DI water bath should be limited. After the substrate was dried with the N<sub>2</sub> gun, it was inspected again under an optical microscope. The photoresist squares must remain on the tops of the remaining SiO<sub>2</sub> squares.

After inspection, the wafer was ready to be etched with the Plasmatherm Inductively-Coupled Plasma Deep Reactive Ion Etcher (ICP-DRIE). This instrument uses the Bosch Process [24] to etch away a deep profile with straight sidewalls and a high aspect ratio. Under any other plasma etching process the etch profile will be isotropic, that is, a pocket will etch evenly in all directions. The micropillar design required an anisotropic etch, where the etch direction is preferentially in one direction (downward) over another (sideways). The Bosch Process achieves anisotropic etching by switching the gases it etches with in a cyclical manner. First, the chamber fills with Ar and SF<sub>6</sub>, with which plasma will generate Ar<sup>+</sup> and CF<sub>3</sub><sup>+</sup> ions that bombard the silicon. Fluorine neutrals (F<sup>0</sup>) chemically combine with the sputtered silicon to create SiF<sub>4</sub>. The SiF<sub>4</sub> then desorbs from the surface, diffuses into the bulk gas and vents out the system. To prevent an isotropic etch profile, a different gas fills the chamber: C<sub>4</sub>F<sub>8</sub>. When plasma is formed with this gas, a Teflon-like polymer (like (C<sub>2</sub>F<sub>4</sub>)<sub>n</sub>) is deposited everywhere on the substrate. When SF<sub>6</sub> is switched back, the ions resulting from the plasma are applied a directional bias that etches the bottom of the trench faster than the sidewalls. Therefore, the sidewalls are protected from further etching,

and the bottom is selectively etched. The  $\text{SF}_6$  and  $\text{C}_4\text{F}_8$  gases are continuously cycled until the desired etch depth is achieved.

The micropillar design called for the towers to be  $75\text{ }\mu\text{m}$  in height. Depending on the mask design, the amount of etch needed to reach 75 microns can vary. For each mask design, the required amount of cycles is shown in Table 2. Typically, if the amount of etchable surface area is reduced, the etch rate will be slower. This effect is commonly called a “loading effect” in ICP-DRIE where the reaction of etching silicon is limited by the transport of Fluorine neutrals to the surface of the material. Loading effect was common in the  $12.5\text{ }\mu\text{m}$  spacing sample since there were many more photoresist squares that composed of the total  $30 \times 30\text{ cm}$  area, reducing the amount of etchable surface area. The etch rate was found by measuring the borders around the edges of each Hybrid Surface with a profilometer, and the minimum tower height is measured since  $75\text{ }\mu\text{m}$  is needed at a minimum.

It should be noted that previous to the mask shown in Figure 7, a different mask was used to make Hybrid Surfaces. This photomask contained “streets” alongside the edges of the samples in the hopes that the wafer would easily break along these pathways. This design would allow easy separation of each design on the wafer. However, the initial etch depth of  $75\text{ }\mu\text{m}$  was not enough of a crack for the wafer to preferentially break along. Therefore, the solution of etching from the

backside was implemented. Nevertheless, values reported here refer to samples made on that mask. The amount of cycles needed to etch with that design is 176.

Due to the cyclic nature of the Bosch Process, the sidewalls of the etch profile will contain a unique profile of many divots, called “scallops.” Due to the isotropic nature of etching with  $\text{SF}_6$ , the etch profile will cut into the sidewalls slightly. As a result, the sidewalls will have a roughness to them. Luckily, this roughness can be calculated. Using an old mixed mask design (with streets) the scallop size was equal to the etch depth per cycle (446 nm). It was approximated that the shape of these scallops are semicircular with a radius of 223 nm. Thus, there is effectively 701 nm of surface length over an effective length of 446 nm, resulting in a Wenzel roughness of  $r_w = 1.57$ . The nanoscale roughness would become a factor when contact angles are measured, increasing the contact angle considerably (similar to the structure of a lotus leaf).

Once the etching process was finished, the wafer was not taken out of a vacuum environment. Exposure of a fresh silicon surface results in a native silicon oxide surface in minutes. First, a layer of hydrophobic material must be deposited on the surface to make the sidewalls and bottom hydrophobic. According to recipe from the ICP-DRIE unit, a plasma of  $\text{C}_4\text{F}_8$  over the surface will deposit approximately 70 nm of Teflon-like material. The Plasma-Enhanced Chemical Vapor Deposition process (PECVD) is already available in the same machine used to etch the wafer.

After the deposition was done, the wafer was taken out, and the chamber was cleaned with an O<sub>2</sub> plasma.

In order to easily separate the samples, an etch on the unpolished side of the wafer was necessary. This etch was done on the STS Advanced Silicon Etcher (also an ICP-DRIE), which also uses the Bosch Process. First, the wafer was marked with a plasma pen over the alignment marks and any holes scratched into the photoresist. Plasma pen markings prevent etching in undesired places and reduce the loading on the machine to etch. It was very important that the etch did not go through the entirety of the wafer. If the wafer was “through-etched” without a protective coating on the polished side, the samples could be left in the chamber and the polished side could overheat, leading to charring the design (effectively destroying it). A protective coating on the polished side was not desired since it could contaminate the nearly completed Hybrid Surface. Therefore, the amount of etchable surface area was reduced to prevent through-etching anywhere. After everything except the window design was covered, the wafer was placed in the etcher and underwent a faster etch than in the Plasmatherm (approximately 14 minutes). The sidewalls of the edges of the samples will be much rougher as a result of the faster etch, but this is inconsequential to the Hybrid Surface structure. The process etched nearly the entire depth of the wafer, allowing for the samples to break apart easily.

The last step before breaking and packaging the samples was the photoresist strip step. AZ 400T photoresist stripper was used to remove the photoresist off the tops of the micropillars. As a result, the Teflon coating on the tops of the towers would also be removed. This process is called “liftoff.” The wafer was submerged in the solvent for 24 hours to allow enough time for the fluid to get underneath the Teflon-like material and dissolve away the photoresist. The wafer was not left in for longer than 24 hours, since 400T is slowly corrosive to the hydrophobic material. Once liftoff was finished, the  $\text{SiO}_2$  tops were exposed, leaving hydrophilic tops. To make sure the leftover Teflon-like squares were completely removed, the wafer was submerged in DI water for 1 minute, followed by a 1:1 mixture of DI water and IPA for 1 minute, then an IPA rinse and  $\text{N}_2$  dry. The samples were broken apart using a diamond scribe and slight pressure on the sides of the samples. The samples were stored in Gel-Pak containers (with gel adhesion level X4), to make sure the surfaces could survive shipping. The unpolished side of the samples stick to the gel with a high amount of surface tension, such that the important features on the front remain untouched during shipping.

#### 4.4 Figures

Table 2: Etch rates for each photomask design

Mask Design	Etch Rate	Cycles to Etch
12.5	0.430 $\mu\text{m}/\text{cycle}$	174
25	0.495 $\mu\text{m}/\text{cycle}$	148
37.5	0.493 $\mu\text{m}/\text{cycle}$	152
50	0.495 $\mu\text{m}/\text{cycle}$	152
mixed	0.396 $\mu\text{m}/\text{cycle}$	190
mixed (old)	0.446 $\mu\text{m}/\text{cycle}$	176

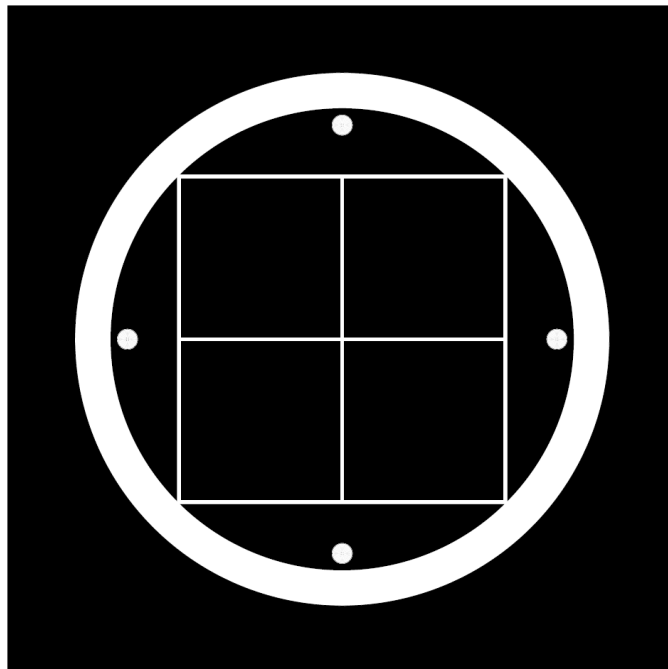


Figure 7: Polished side design photomask

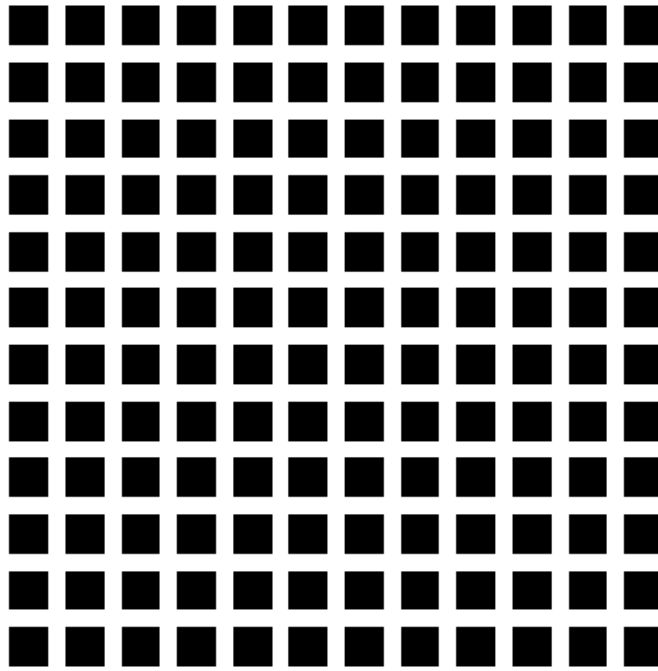


Figure 8: Zoom picture of one quadrant of the mask design

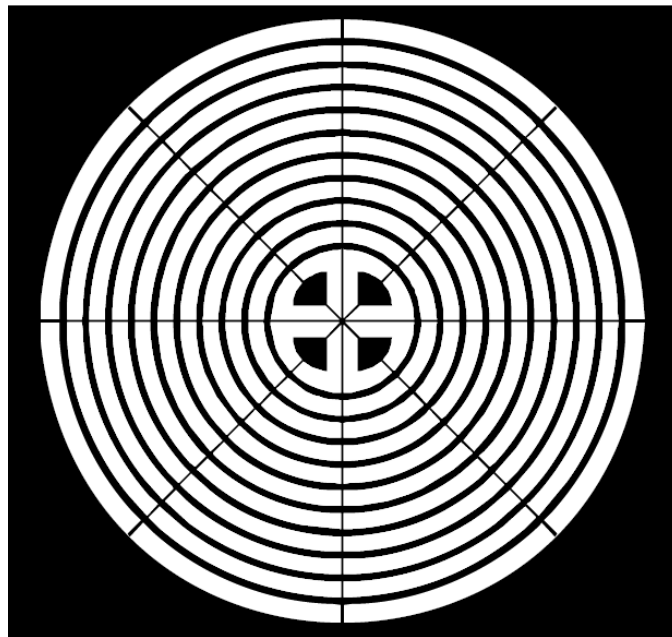


Figure 9: A fiducial (alignment) mark

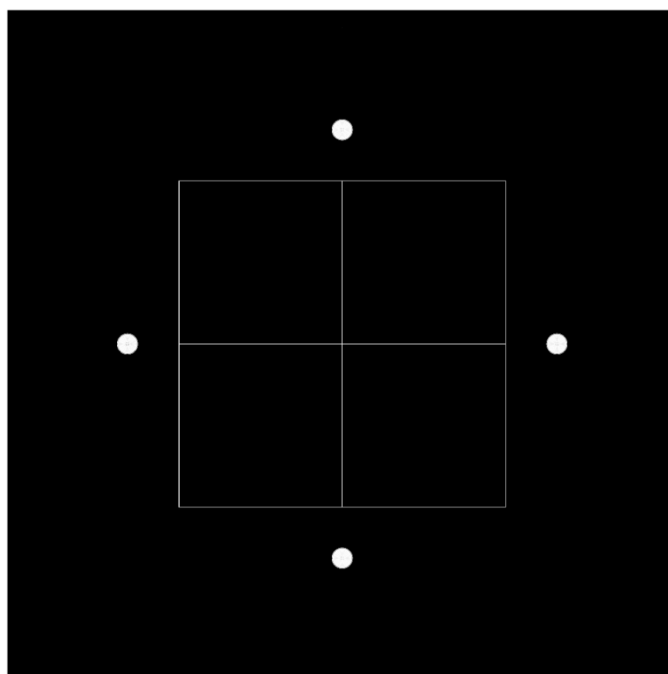
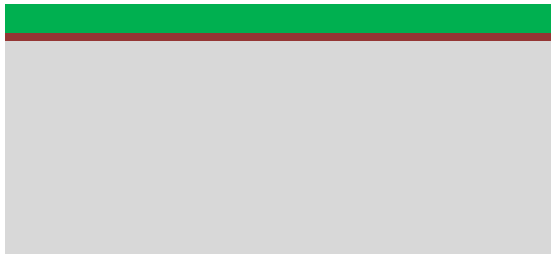


Figure 10: Unpolished side window mask

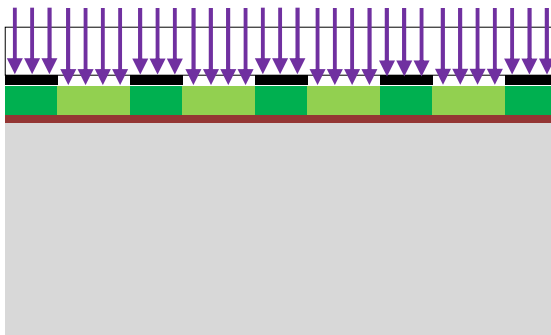




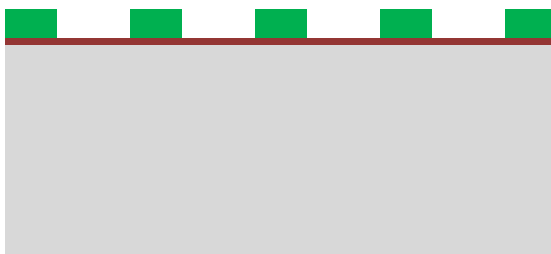
Spin photoresist, soft bake resist to prevent adherence during mask alignment.



Align mask to resist, align mask to fiducial marks, if needed.



Expose with 405 nm light for 12 seconds, photoresist undergoes scissioning.



Submerge in AZ 400K developer, exposed resist dissolves away, leaving pattern behind.

Figure 11: A sample photolithography process

## CHAPTER 5: CHARACTERIZATION

Once fabrication was complete, the finished surfaces underwent characterization of their structure, composition, and surface energy characteristics. Pillar height was measured using a profilometer, images were obtained using a Scanning Electron Microscope (SEM), identification of composition was facilitated using Energy-Dispersive X-Ray Spectroscopy (EDX) and Time-of-Flight Secondary Ion Mass Spectrometry (TOF-SIMS), and the contact angle was measured with a goniometer.

### 5.1 Profilometry

In order to find the height of the towers, a profilometer was used to measure the edges around the Hybrid Surfaces. Since the towers are too small to measure with the needle of the profilometer, the etch depth was measured on larger features around the surface. For instance, if the depth of the towers on the top-left of the wafer needed to be known (see Figure 7), measurements were obtained on the opposite edge above or to the left of the sample. Due to the non-uniformity of the ICP-DRIE etch the etch depth will not be consistent across the entire wafer. Depending on location, one wafer can have a depth range of 78 to 92  $\mu\text{m}$ . For better Cassie-Baxter state stability, the aspect ratio of the towers must be high. Therefore, the important measurement to note is the minimum depth, since the towers will be at least this tall.

## 5.2 Scanning Electron Microscopy

Tower top dimensions and sidewall condition were visualized using an SEM. For each surface, images were obtained at X550 magnification and 5 kV electron energy. A top view of each type of surface was obtained to get tower width values (a) and spacing values (b) (Figures 12-15). Table 3 summarizes these values compared to the expected values. Notice the dimensional accuracy of the space between towers becomes worse as the spacing gets closer to the resolution limit ( $\sim 7 \mu\text{m}$ ). In addition to verifying tower dimensions, the sidewalls were inspected. In Figure 16 it was very apparent that scallops form on the sidewalls due to the ICP-DRIE process. The size of these scallops are orders of magnitude smaller than the overall tower height, but they are not negligible. As explained earlier, the Wenzel roughness of these sidewalls is  $r_w = 1.57$ .

## 5.3 Energy-Dispersive X-Ray Spectroscopy

Following SEM analysis, EDX was used to verify the materials on the tower tops and sidewalls. The SEM was pointed toward each of these features and a spectrum was recorded. Electrons will hit the surface, which emits an X-Ray for the EDX instrument to detect. The energy of the X-Ray corresponds to a specific element, which allows the identification of material composition. For the tower tops (Figure 17) only silicon and oxygen are detected, which means the tower tops are purely  $\text{SiO}_2$ , as expected. In addition, the tower sidewalls (Figure 18) show signatures of carbon and fluorine, which verified the composition of the sidewalls

containing a fluorocarbon. Signatures of silicon and oxygen were still detected for two reasons: some of the tower top was in focus for this measurement, and the electrons will still penetrate the surface and give identification of materials underneath the hydrophobic material.

#### 5.4 Time-of-Flight Secondary Ion Mass Spectroscopy

In addition to EDX, TOF-SIMS can also verify the chemical composition of a Hybrid Surface. It works by sending pulsed gold ions to the surface of the sample, which removes molecules from the surface and sends them into a “flight tube.” Depending on how long it takes to reach the detector (a function of mass), the element can be identified. The advantage to this method is a visual representation of where specific elements are. In Figure 19, an example of TOF-SIMS imaging is provided on a 50  $\mu\text{m}$  spacing Hybrid Surface. The first image is total counts recorded. If one section of the image is dimmer than another, it may only mean that fewer counts were recorded. The color red is assigned to any fluorine signatures that appear. Notice that most of the red surrounds towers, but are not on the tower tops. Instead, a green signature is evident, which signifies oxygen. This result corroborates the findings from EDX, a fluorine signature ( $(\text{C}_2\text{F}_4)_n$ ) covers the tower sidewalls and base, and an oxygen signature ( $\text{SiO}_2$ ) covers the tower tops.

## 5.5 Goniometry

The main characterization of wettability is obtained with a goniometer. A goniometer was used to measure contact angle which is directly related to interfacial free energy, as discussed earlier. Measurements with DI water placed on the surface were recorded for a multitude of surfaces: flat  $\text{SiO}_2$ , flat hydrophobic material, and Hybrid Surfaces. Advancing and receding angle were primarily recorded since these values provide a more complete characterization than simple equilibrium, sessile-drop contact angles. However, equilibrium angles were also recorded on the Hybrid Surfaces.

In order to measure advancing angles, an initial droplet of about 9  $\mu\text{L}$  was deposited onto the surface. With the tip of the pipet still contacting the droplet, the pipet was raised until it barely contacted the droplet. The pipet was positioned towards the center of the droplet. The goniometer starts taking images when the pipet starts dispensing water at 0.5  $\mu\text{L/s}$ . The goniometer records 1 image per second. When the TCL moved, the advancing angle was recorded. Many values may be recorded in the same test, as long as the TCL continues to move. For each test, a plot was constructed of contact angle over time (Figure 20). When the TCL moved, the contact angle remained constant. The data points on this flat part of the curve are averaged and a standard deviation was calculated. Once the tests were completed, a cumulative average and standard deviation of all the tests was calculated.

Measurements of the receding angle were obtained in a similar way, except the tip of the pipet was moved as close to the surface as possible. It was also necessary to move the stage such that the tip remained in the center of the droplet. When the pipet starts to take in water at 0.5  $\mu\text{L/s}$ , the goniometer starts recording images. Every 33 ms an image was obtained, since the receding droplet TCL moves with a higher velocity than does an advancing TCL. There are two common ways used to measure the receding angle depending on surface roughness. For a smooth surface the measurement is taken as it is for the advancing angle, where the value does not change over time and an average is calculated. On the other hand, for a micropillar surface, the receding angle can only be measured when the droplet TCL moves from tower to tower. As described in Chapter 3, pinning is observed during a receding angle measurement. If an average were calculated over time, frames will be recorded where there is no TCL movement. Thus, the recorded value turns out to be a few degrees larger than the correct receding angle—clearly incorrect. The video from the goniometer was reviewed frame by frame until TCL movement was observed. The contact angle just before and after TCL motion was recorded. Just as with the advancing angle, each test had its own respective average and standard deviation, and a cumulative average of all tests was used as the final value.

During measurements of the equilibrium contact angle, the contact angle of the droplet will fall between the values of advancing and receding angle. If the contact angle hysteresis is large enough, the observed contact angle can depend on how the droplet was deposited on the surface [19, 25]. For the current experiments, the droplets were deposited with the TCL on an advancing front. Each droplet had a size of about  $9 \pm 0.62 \mu\text{L}$ . The pipet was lowered until the droplet stuck to the surface, and it was then lifted high enough for the droplet to separate and settle. In every sessile drop experiment, the number of towers the droplet initially stuck to was always less than the number of towers the droplet eventually settled on. Therefore, these droplets had an advancing front, which caused the contact angle to be closer to advancing angle than receding angle. The results of advancing, receding, and equilibrium angles are compared to theory in Chapter 6.

## 5.6 Figures

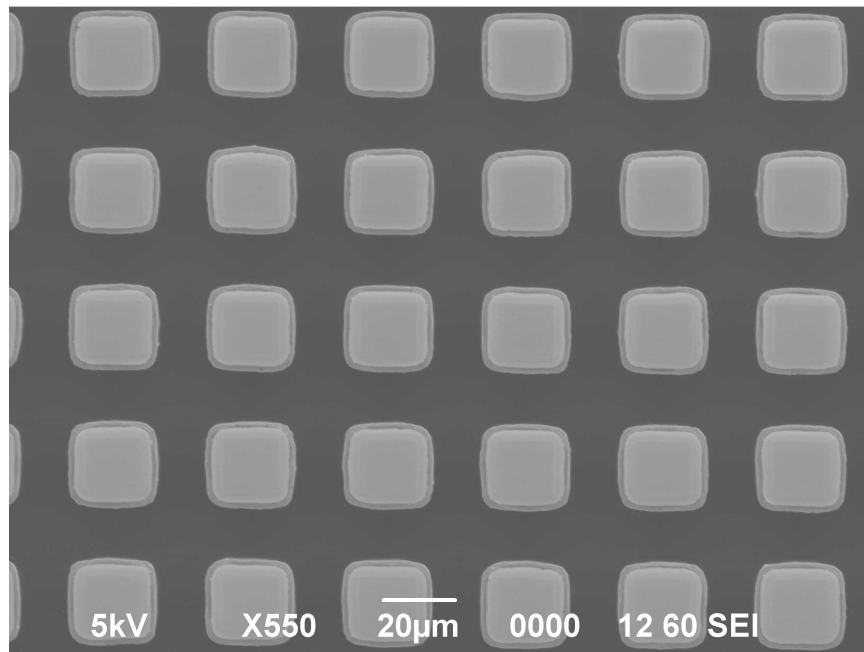


Figure 12: 12.5  $\mu\text{m}$  spacing Hybrid Surface [26]

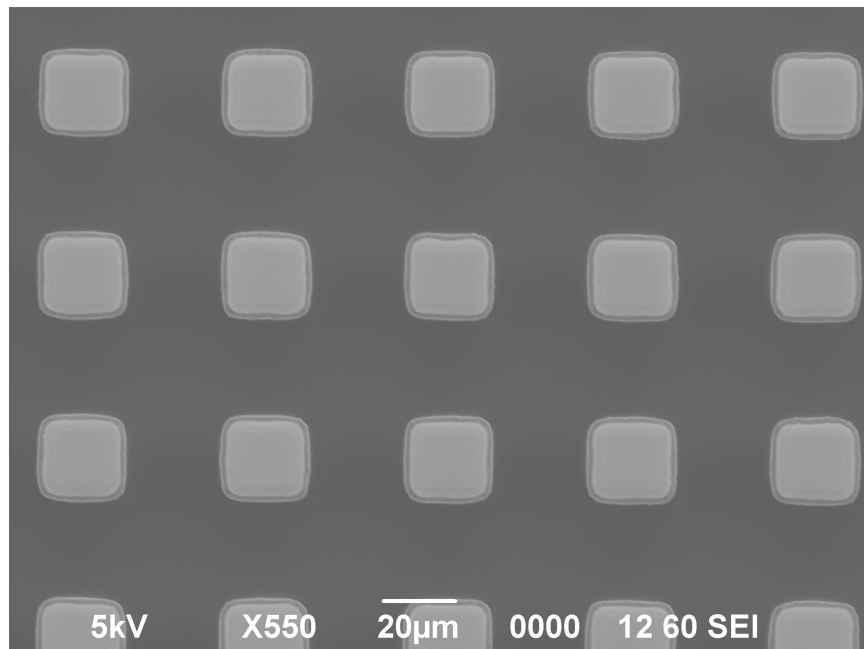


Figure 13: 25  $\mu\text{m}$  spacing Hybrid Surface [26]



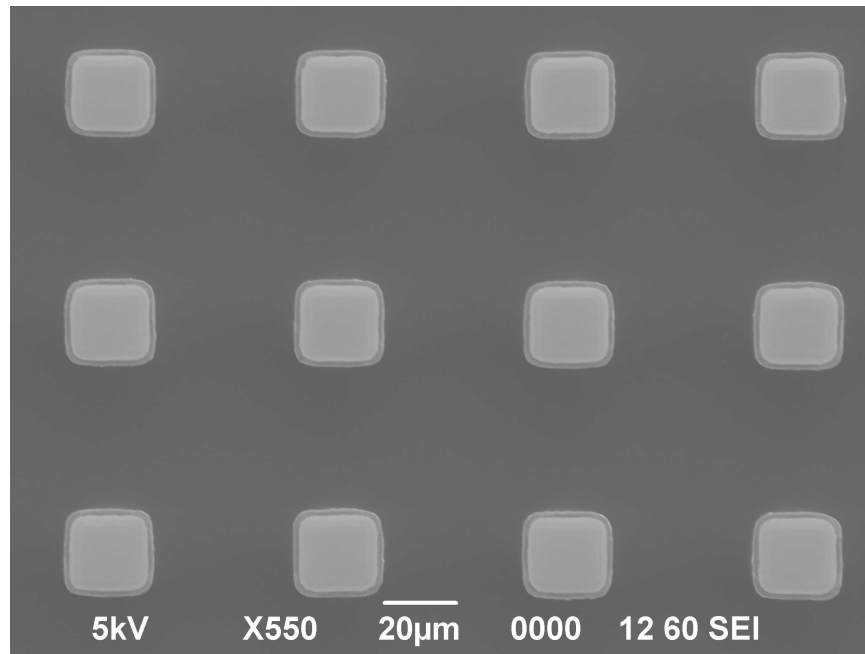


Figure 14: 37.5  $\mu\text{m}$  spacing Hybrid Surface [26]

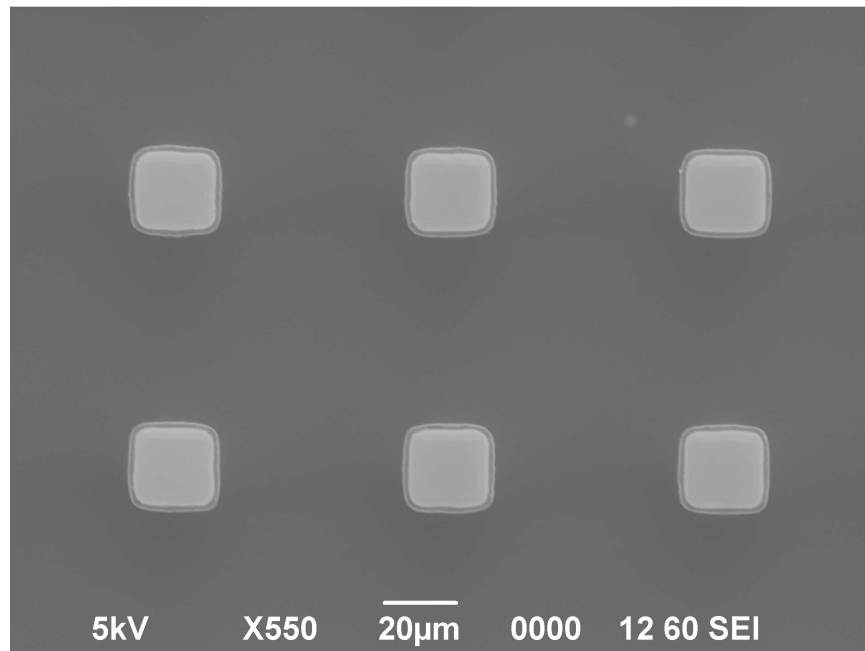


Figure 15: 50  $\mu\text{m}$  spacing Hybrid Surface [26]

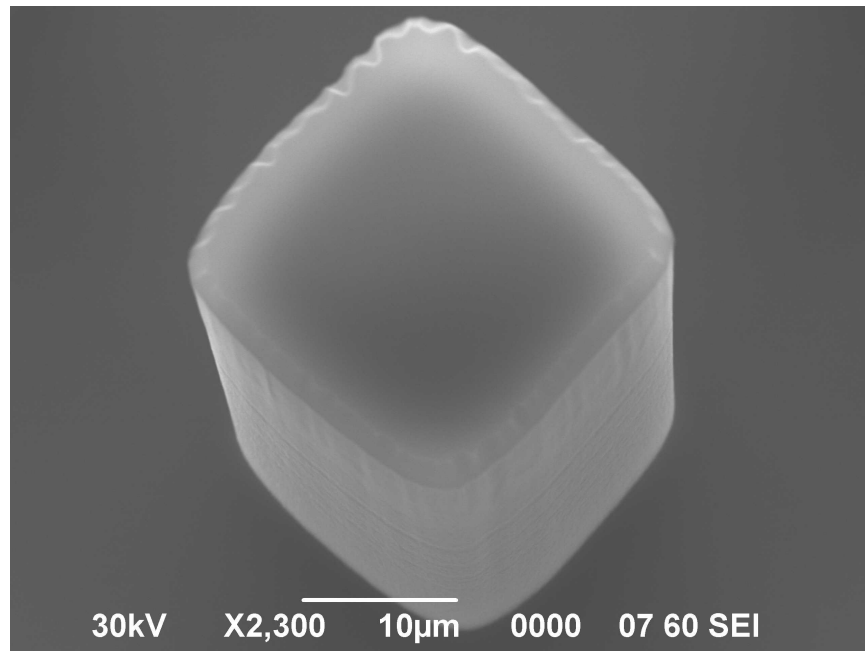


Figure 16: Single tower SEM picture

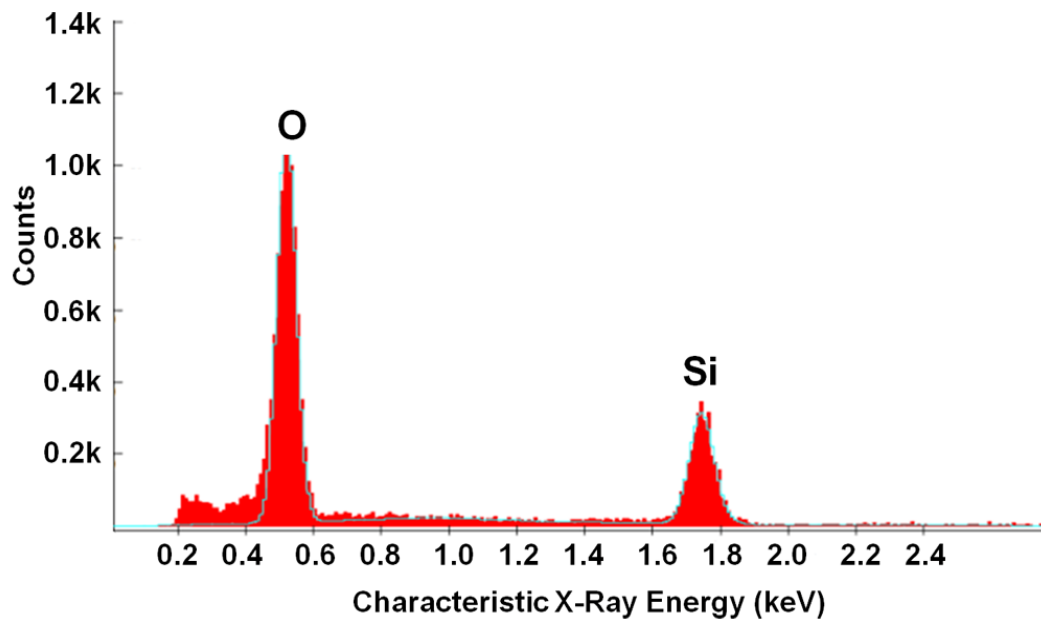


Figure 17: EDX spectrum of a micropillar top [26]

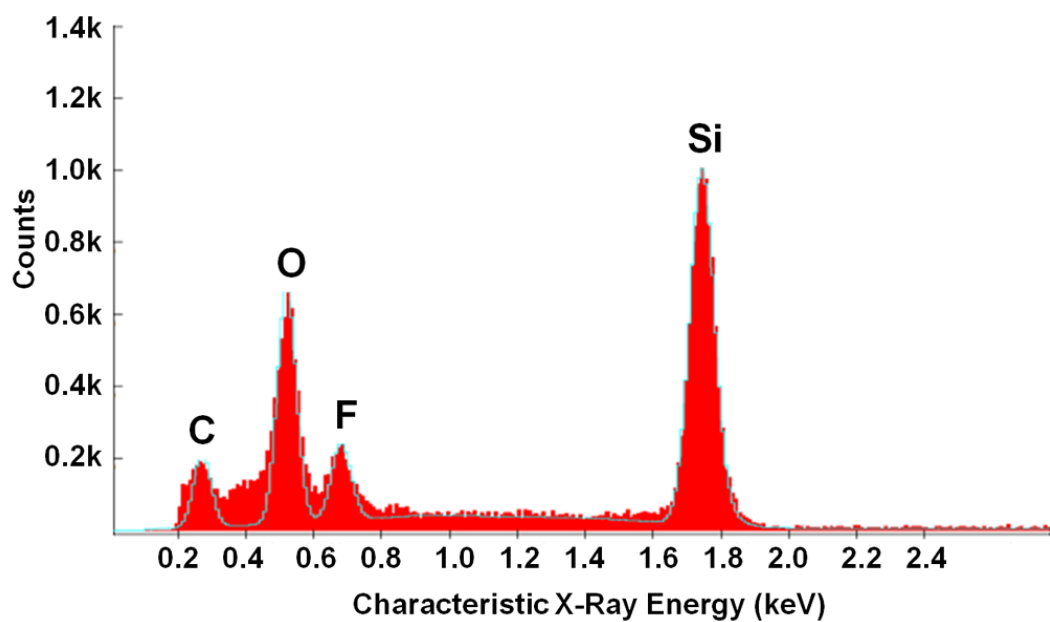


Figure 18: EDX spectrum of a micropillar sidewall [26]

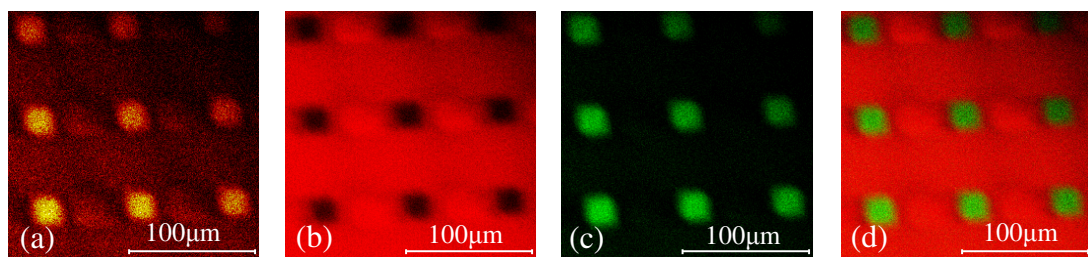


Figure 19: TOF-SIMS of a Hybrid Surface (a) Total counts (yellow), (b) Fluorine location (red), (c) Oxygen location (green), (d) Oxygen and Fluorine overlay [26]

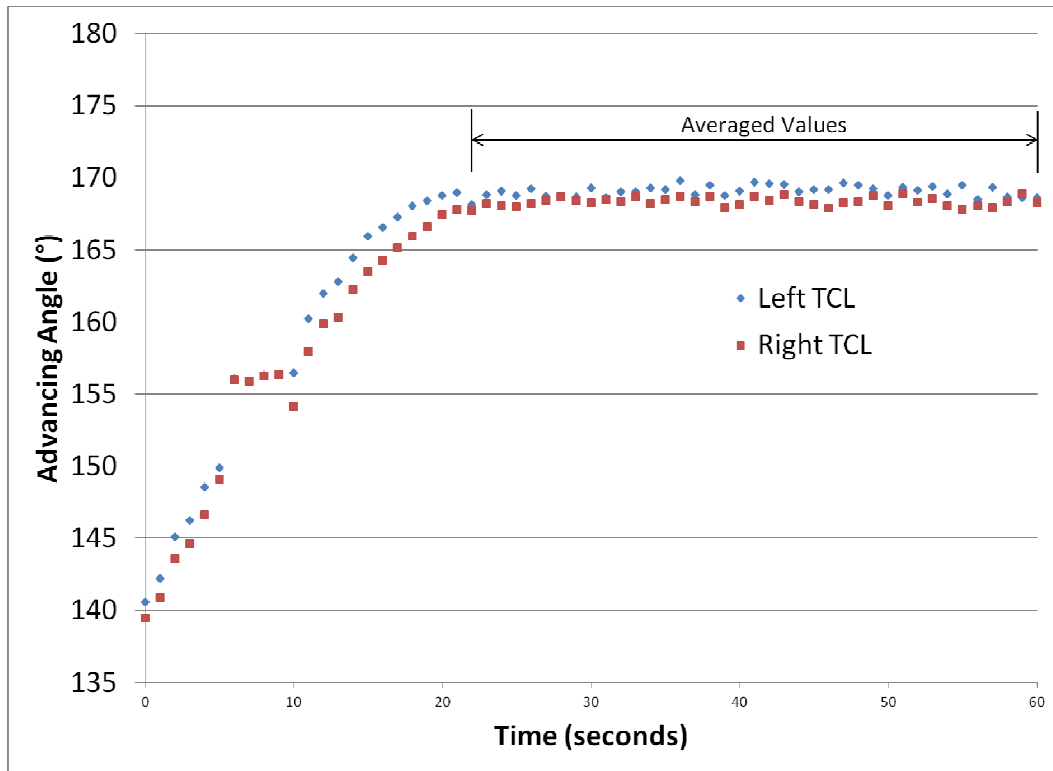


Figure 20: Example of advancing angle measurement.

Table 3: Actual tower dimensions

Design	a	a % error	b	b % error
12.5 spacing	24.11	3.6%	14	12%
25 spacing	22.83	8.7%	24	4.0%
37.5 spacing	23.23	7.1%	38	1.3%
50 spacing	24.63	1.5%	49	2.0%

## CHAPTER 6: RESULTS AND DISCUSSION

### 6.1 Factors in the contact angle model

Advancing, receding, and equilibrium angle measurements were obtained and compared to the Cassie-Baxter and Wenzel equations. Equations (2) and (3) were utilized for Wenzel and Cassie-Baxter state, respectively. In order to generate a reliable model, some factors related to the geometry needed to be taken into consideration.

The intrinsic contact angle of a Hybrid Surface tower top was one factor needed for the model. On the tower top, the center is covered by SiO<sub>2</sub> (a majority) and the edges will have some Teflon-like material deposited. Determining the intrinsic angle of this structure is difficult because a flat version of this structure is not comparable. On the other hand, prior work by others weighted the contact angles of both surfaces as a function of their area fractions to determine this contact angle, much like the Cassie-Baxter equation with solid and air interfaces. They all have a similar result, with the equation [7, 8, 26-28]

$$\cos \theta_{1e} = x_1 \cdot \cos \theta_1 + x_2 \cdot \cos \theta_2 \quad (6)$$

Where  $\theta_{1e}$  is the effective angle of the tower tops,  $\theta_1$  is the contact angle of SiO<sub>2</sub>,  $x_1$  is the area fraction of hydrophilic material,  $\theta_2$  is the contact angle of the

hydrophobic material, and  $x_2$  is the area fraction of hydrophobic material. Because the thickness of the Teflon-like material is very small (approximately 70-80 nm) the value of  $x_2$  is very small, between 0.0057 and 0.0062. Nevertheless, it was taken into account.

Modifications needed to be made to equations (2) and (3) in order to be applied to a Hybrid Surface model. Starting with Wenzel's equation, the apparent contact angle of a Hybrid Surface can be found with the following equation [26]

$$\cos \theta_W = f_1(\cos \theta_{1e} - \cos \theta_2) + R \cdot \cos \theta_2 \quad (7)$$

where  $R$  is a function of tower geometry

$$R = 1 + \frac{4 \cdot h}{a \cdot \left(1 + \frac{b}{a}\right)^2} \quad (8)$$

and  $h$  is the tower height. The Cassie-Baxter equation does not change as much; it is only modified for the effective intrinsic angle of the tower sidewalls  $\theta_{SW}$  (in a advancing angle prediction)

$$\cos \theta_{CB} = f_1 \cos \theta_{SW} - f_2 \quad (9)$$

or the effective intrinsic angle of the tower tops (in a receding angle prediction)

$$\cos\theta_{CB} = f_1\cos\theta_{1e} - f_2 \quad (10)$$

Where the solid-liquid interface area fraction is

$$f_1 = \frac{a^2}{(a+b)^2} \quad (11)$$

and the air-liquid interface area fraction is

$$f_2 = 1 - f_1 \quad (12)$$

Equations (7), (9), and (10) required the contact angles of both flat SiO<sub>2</sub> and flat (C<sub>2</sub>F<sub>4</sub>)<sub>n</sub>. Those respective contact angles require additional analysis to account for surface cleanliness and roughness.

After liftoff, the flat SiO<sub>2</sub> surfaces left around the Hybrid Surface were measured for their advancing and receding angles. A completely clean SiO<sub>2</sub> wafer was not chosen for this measurement, because it was not representative of the cleanliness of the tops of the towers. The towers (and this flat SiO<sub>2</sub> section of the wafer) were covered in photoresist, which was blanketed with hydrophobic material, then cleaned off by AZ 400T. This surface condition was not the same as a newly oxidized or freshly plasma cleaned surface, which may exhibit contact angles of 0 degrees. The surfaces of these SiO<sub>2</sub> sections have a higher contact angle than a

completely clean surface. The advancing and receding angles for flat SiO<sub>2</sub> are shown in Table 4.

In order to obtain the intrinsic angle of the Teflon-like material, a clean silicon wafer was placed inside the Plasmatherm ICP-DRIE and a one-minute deposition step was completed, depositing approximately 70 nm of hydrophobic material on the surface. A clean silicon wafer was used because it was the smoothest available surface to test, since any large degree of roughness can cause the contact angle to increase. For instance, hydrophobic material on photoresist exhibited an advancing angle of nearly 160 degrees. Any nanoscale roughness will cause this value to increase. The advancing and receding angles for the hydrophobic material are also shown in Table 4. In addition to the intrinsic angle, there was a measurable roughness on the sidewalls. As described in Chapter 4, the Wenzel roughness of the sidewalls is approximately 1.57. If this value is used in equation (2), the Wenzel angle will change. This Wenzel angle is the real contact angle of the sidewalls, which will be used in the model.

## 6.2 Advancing angle

In Figure 21, the measured values of advancing angle are plotted against Wenzel and Cassie-Baxter theories. The general agreement with Cassie-Baxter theory with the experimental data suggests that droplets rest in a composite state. It also shows that the degree of hydrophobicity on the sidewalls has a drastic effect on



advancing angle. When the droplet remains “pinned” to the side of a micropillar, the increase in droplet volume will only increase the contact angle more. Pinning to the sides of asperities is widely documented in literature [21, 29, 30]. In addition, Extrand also mentions that during this pinning phenomenon, the droplet TCL moves to the sidewalls of the asperities, exhibiting the advancing angle of the sidewalls [31]. This behavior is shown in Figure 21. When using the advancing angle of flat  $(\text{C}_2\text{F}_4)_n$  ( $\theta_{sw} = 125.5^\circ$ ), the model vastly underestimates the value of advancing angle. Only when Wenzel roughness of the sidewalls was taken into account ( $\theta_{sw} = 155.9^\circ$ ) was where the model will agree with experimental values.

The droplet will only advance once the free energy barrier is overcome, which requires enough energy to move the TCL across the large air gap. Free energy barriers can exist particularly on heterogeneous surfaces where hydrophilic regions alternate with hydrophobic regions across the surface [7]. The hydrophobic region, for example, could be an air gap across two towers or a hydrophobic strip between hydrophilic regions. Morita *et al.* observed an anisotropic wetting phenomena on a surface of hydrophobic and hydrophilic strips, because of this energy barrier to TCL movement across the strips [28]. Because of this free energy barrier between towers, metastable states can exist. Droplets of the same volume can remain stable contacting a different number of towers. If the droplet remains stable while contacting more towers, the contact

angle will be lower than if the droplet settles on fewer towers. These barriers have a slight effect on advancing angle, seen in Figure 21. If this gap distance increases (i.e. when the tower spacing increases) the energy barrier becomes larger and the advancing angle will increase.

### 6.3 Receding angle

Figure 22 shows the receding angle plotted against tower spacing. Along with the plots of Wenzel and Cassie-Baxter models, the experimental data are shown. There are two sets of experimental values, which are maximum and minimum receding angles. The minimum angle occurs right before TCL movement to the next tower. The maximum angle was recorded immediately after TCL movement. The common definition of receding angle is the contact angle just before TCL movement, which will correspond to the minimum value. This jump in contact angle from tower to tower is also a result of pinning since a free energy barrier exists in movement of the TCL between towers, regardless of direction.

The trend of experimental values compared to both models suggests once again that the droplets settle in a Cassie-Baxter equilibrium state, since receding angles increase with tower pitch. Experimental results similar to these have been presented by Furstner and Barthlott [20] as well as Bhushan and Jung [30]. Note that there is a larger variation in receding angles than advancing angles. Drelich *et al.* explain that the advancing angle is less sensitive to the solid structure than is

the receding angle, which makes the receding angle a more reliable metric for determining surface structure parameters such as tower spacing [32].

#### 6.4 Equilibrium angle

The equilibrium angle is described as the contact angle of an undisturbed droplet in its lowest energy state. Due to the hysteretic nature of the contact angle on Hybrid Surfaces, the equilibrium contact angle may be hard to determine. Many metastable states will exist as a sessile drop settles on a surface, which can provide significant variability in recorded values (as described in Chapter 5). A plot of experimental equilibrium angles is presented in Figure 23. It has been suggested that a theoretical value of equilibrium angle  $\theta_{eq}$  can be determined by averaging the advancing ( $\theta_{adv}$ ) and receding ( $\theta_{rec}$ ) values [26]

$$\theta_{eq} = \frac{\theta_{adv} + \theta_{rec}}{2} \quad (13)$$

In the current work, this approach was adopted by predicting the advancing contact angle using Equation (9), with  $\theta_{sw}$  equivalent to the contact angle of the sidewalls accounting for its Wenzel roughness ( $\theta_{sw} = 155.9$ ). The receding contact angle was predicted using Equation (10), with  $\theta_{le}$  calculated using Equation (6), referencing  $\theta_1$  and  $\theta_2$  as the receding angles of flat SiO<sub>2</sub> and Teflon, respectively (see Table 4). The results are provided along with the measured values in Figure 23. The error bars for the data were derived from another

experiment in which water was added to the droplet in increments of about 0.5  $\mu\text{L}$ , followed by an experiment where water was subtracted in increments. This procedure provided a measure of the range of equilibrium states possible with each surface. For the 12.5  $\mu\text{m}$  spacing surface, there was greater variability in equilibrium angle. This variability might be caused by either a larger quantity of towers to contact (many more equilibrium states possible) or a larger hysteresis value which may mean the surface has larger free energy barriers to cross, and thus droplets get “lodged” in metastable states away from the global energy minimum. The large amount of hydrophilic area in contact with the droplet may cause a large energy barrier. It is noteworthy that each of the averaged experimental values are nearer the higher limit of equilibrium angle, because each sessile drop experiment was conducted with an advancing TCL front, as explained in Chapter 5.

## 6.5 Figures

Table 4: Advancing and receding angles of flat Teflon and SiO<sub>2</sub>

Material	Advancing	Receding	Equilibrium (Eq. 13)
Teflon	125.6°	98.6°	112.1°
SiO <sub>2</sub>	40.6°	7.0°	23.8°

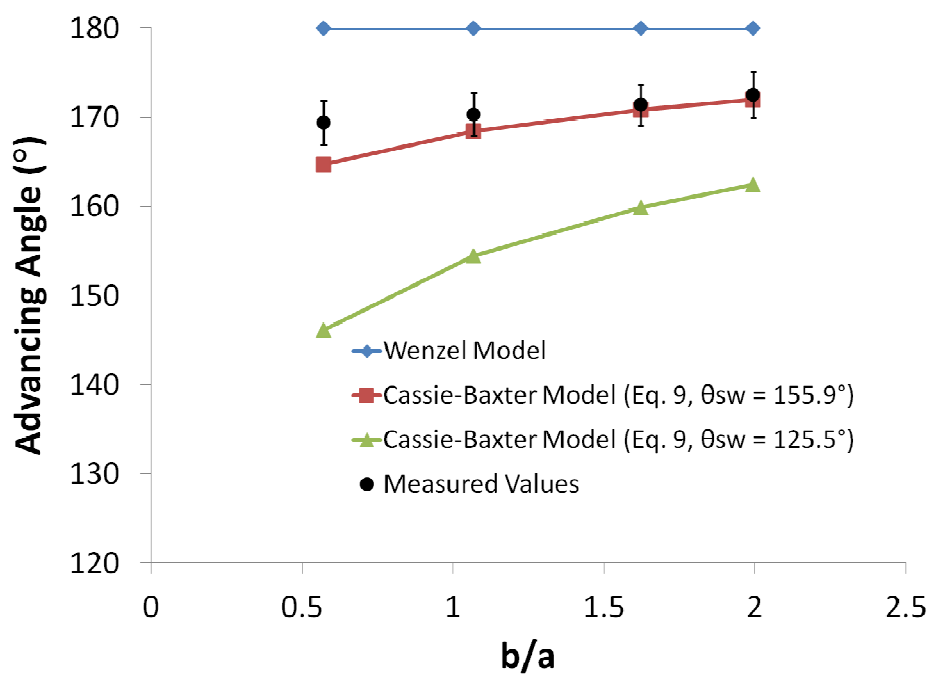


Figure 21: Advancing angle of Hybrid Surfaces

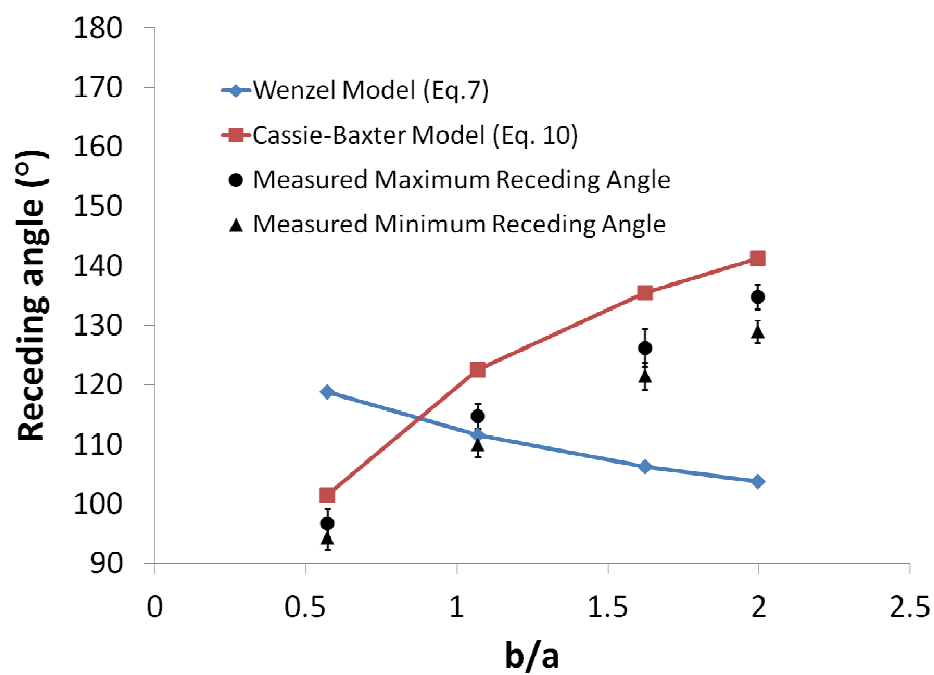


Figure 22: Receding angle of Hybrid Surfaces

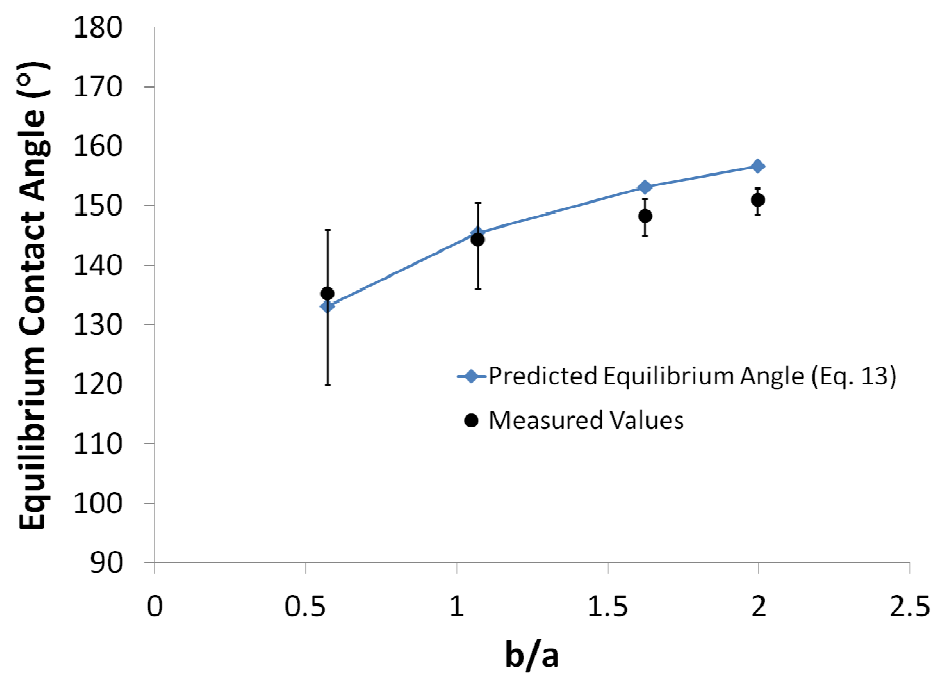


Figure 23: Equilibrium angle of Hybrid Surfaces [26]

## CHAPTER 7: FUTURE WORK

### 7.1 Objectives

In the final year of the project, the required milestones include a model of drop formulation and dynamics, along with exploring the use of surface vibration to remove droplets. The model is expected to be a semi-theoretical model, so experimental data are needed. With the new Hybrid Surfaces designed, fabricated and characterized at the University of Illinois, the studies of droplet nucleation, growth and coalescence will be conducted at the Texas A&M University. In this chapter, ideas and recommendations related to the continuation of the work are presented.

### 7.2 Droplet nucleation

Varanasi *et al.* describe how Hybrid Surfaces benefit from precise placement of hydrophobic and hydrophilic surfaces [14, 15]. For each type of surface, there is a free energy barrier to nucleation  $\Delta G$  (assuming a droplet with a large enough critical radius) is given by [33]

$$\Delta G = \frac{4}{3}\pi r_e^3 \gamma^{LA} F_\theta \quad (14)$$

where

$$F_{\theta} = \frac{2-3 \cos \theta_{eq} + \cos^3 \theta_{eq}}{4} \quad (15)$$

and  $r_e$  is the critical radius. Assuming a constant critical radius and subcooling temperature, this equation implies that the hydrophobic surfaces ( $\theta_{eq} = 112^\circ$ ) have a nucleation energy barrier over 145 times larger than that of the hydrophilic surfaces ( $\theta_{eq} = 24^\circ$ ). Of course, if the subcooling temperature is low enough, water will condense anywhere on the surface, and that may cause droplets to start in the Wenzel mode. The nucleation rate is related to the contact angle through the following relation [33]

$$J \propto \frac{F_{\theta}^{\frac{3}{2}} (1 - \cos \theta_{eq})}{\exp F_{\theta}^3} \quad (16)$$

which suggests embryos are formed on a hydrophilic surface at a rate that is nearly 17,500 times that of the hydrophobic surface. Typically, a threshold value is assumed for  $J$ , and once conditions are such that the threshold is exceeded, it is expected that nucleation will proceed. Again, if the subcooling temperature is low enough, many droplets may be able to nucleate on the hydrophobic material, only they would nucleate slower than on hydrophilic material.



### 7.3 Dropwise condensation heat transfer

Filmwise condensation is disadvantageous in heat transfer because the thin film offers a heat transfer resistance. In addition to heat flowing through the solid surface, conduction through water is also necessary. Even during dropwise condensation this conduction resistance can be important for large droplets. For efficient dropwise condensation, droplet diameters typically need to be less than 10  $\mu\text{m}$  [34]. A truly significant enhancement could be achieved if droplets of 10  $\mu\text{m}$  diameter and larger roll off the surface, but this is very difficult to accomplish. Coalescence usually occurs before droplets are large enough to roll off the surface from gravity alone. Typically, a droplet coalesces to a diameter of 2-5 mm in diameter before rolling off a vertical surface [34].

Experimental methods should find the maximum droplet diameters possible before roll off for each surface. When the maximum diameters are known, the amount of surface area covered by droplets can be found through the relation provided by Rose [35]

$$A(r)dr = \left(\frac{1}{3}\right) \cdot \left(\frac{r}{r_{max}}\right)^{-2/3} \cdot \frac{dr}{r_{max}} \quad (17)$$

Following Rose, the results can then be used to find a prediction of the average heat flux of the surface

$$q = \int_{r_e}^{r_{max}} \left\{ \frac{\frac{\Delta T}{T} - \frac{2\sigma}{r\rho h_{fg}}}{\left( \frac{2r}{3\lambda T} + \frac{1}{2\rho_v h_{fg}^2} \right) \cdot \left( \frac{\gamma+1}{\gamma-1} \right) \cdot \left( \frac{R_g T}{2\pi} \right)^{\frac{1}{2}}} \right\} A(r) dr \quad (18)$$

An experimental analysis similar to that of Dietz *et al.* would be advantageous to this study [36]. An area fraction of droplets smaller than 10  $\mu\text{m}$  can be found, which can be used to approximate the surface heat flux. Introduction of vibration may also be advantageous, as it may promote coalescence and droplet roll at diameters smaller than those removed by gravity alone. The heat flux due to dropwise condensation can be compared to that obtained for flat silicon surfaces and a plain towered silicon surface as a control to measure the degree of benefit in heat flux, giving some insight into the promise of these surfaces in application.

## REFERENCES

1. Kandlikar, S.G., M. Shoji, and V.K. Dhir, *Handbook of phase change: boiling and condensation* 1999: Taylor & Francis.
2. Ma, X., J.W. Rose, D. Xu, J. Lin, and B. Wang, *Advances in dropwise condensation heat transfer: Chinese research*. Chemical Engineering Journal, 2000. **78**(2-3): p. 87-93.
3. Young, T., *An Essay on the Cohesion of Fluids*. Philosophical Transactions of the Royal Society of London, 1805. **95**(ArticleType: research-article / Full publication date: 1805 /): p. 65-87.
4. Wenzel, R.N., *Resistance of solid surfaces to wetting by water*. Industrial and Engineering Chemistry, 1936. **28**: p. 988-994.
5. Cassie, A.B.D. and S. Baxter, *Wettability of porous surfaces*. Transactions of the Faraday Society, 1944. **40**: p. 546-551.
6. Shuttleworth, R. and G.L.J. Bailey, *The spreading of a liquid over a rough solid*. Discussions of the Faraday Society, 1948(3): p. 16-22.
7. Johnson, R.E. and R.H. Dettre, *Contact Angle Hysteresis. III. Study of an Idealized Heterogeneous Surface*. The Journal of Physical Chemistry, 1964. **68**(7): p. 1744-1750.

8. Dettre, R.H. and R.E. Johnson, Jr., *Contact angle hysteresis. IV. Contact angle measurements on heterogeneous surfaces*. Journal of Physical Chemistry, 1965. **69**(5): p. 1507-1515.
9. Good, R.J., *A Thermodynamic Derivation of Wenzel's Modification of Young's Equation for Contact Angles; Together with a Theory of Hysteresis*. Journal of the American Chemical Society, 1952. **74**(20): p. 5041-5042.
10. Johnson Rulon, E. and H. Dettre Robert, *Contact Angle Hysteresis*, in *Contact Angle, Wettability, and Adhesion* 1964, AMERICAN CHEMICAL SOCIETY. p. 112-135.
11. Dettre Robert, H. and E. Johnson Rulon, *Contact Angle Hysteresis*, in *Contact Angle, Wettability, and Adhesion* 1964, AMERICAN CHEMICAL SOCIETY. p. 136-144.
12. Chen, W., A.Y. Fadeev, M.C. Hsieh, D. Oner, J. Youngblood, and T.J. McCarthy, *Ultrahydrophobic and ultralyophobic surfaces: some comments and examples*. Langmuir, 1999. **15**(10): p. 3395-3399.
13. Barthlott, W. and C. Neinhuis, *Purity of the sacred lotus, or escape from contamination in biological surfaces*. Planta, 1997. **202**(1): p. 1-8.

14. Varanasi, K.K., H. Ming, N. Bhate, Y. Wensha, and D. Tao, *Spatial control in the heterogeneous nucleation of water*. Applied Physics Letters, 2009. **95**(9): p. 094101 (3 pp.).
15. Varanasi, K.K. and T. Deng. *Controlling nucleation and growth of water using hybrid hydrophobic-hydrophilic surfaces*. in *2010 12th IEEE Intersociety Conference on Thermal and Thermomechanical Phenomena in Electronic Systems, ITherm 2010, June 2, 2010 - June 5, 2010*. 2010. Las Vegas, NV, United states: IEEE Computer Society.
16. Hozumi, A. and O. Takai, *Preparation of ultra water-repellent films by microwave plasma-enhanced CVD*. Thin Solid Films, 1997. **303**(1-2): p. 222-225.
17. Yabu, H. and M. Shimomura, *Single-step fabrication of transparent superhydrophobic porous polymer films*. Chemistry of Materials, 2005. **17**(21): p. 5231-5234.
18. Thomas, R.R., F.B. Kaufman, J.T. Kirleis, and R.A. Belsky, *Wettability of polished silicon oxide surfaces*. Journal of the Electrochemical Society, 1996. **143**(2): p. 643-648.
19. Patankar, N.A., *On the modeling of hydrophobic contact angles on rough surfaces*. Langmuir, 2003. **19**(4): p. 1249-1253.

20. Furstner, R., W. Barthlott, C. Neinhuis, and P. Walzel, *Wetting and self-cleaning properties of artificial superhydrophobic surfaces*. Langmuir, 2005. **21**(3): p. 956-961.
21. Nosonovsky, M. and B. Bhushan, *Roughness optimization for biomimetic superhydrophobic surfaces*. Microsystem Technologies, 2005. **11**(7): p. 535-549.
22. Madou, M.J., *Fundamentals of microfabrication: the science of miniaturization* 2002: CRC Press.
23. Deal, B.E. and A.S. Grove, *General Relationship for the Thermal Oxidation of Silicon*. Journal of Applied Physics, 1965. **36**(12): p. 3770-3778.
24. Laermer, F. and A. Schilp, *Method of anisotropically etching silicon*, 1996, Robert Bosch GmbH (Stuttgart, DE): United States.
25. He, B., N.A. Patankar, and J. Lee, *Multiple equilibrium droplet shapes and design criterion for rough hydrophobic surfaces*. Langmuir, 2003. **19**(12): p. 4999-5003.
26. Yao, C.W., T.P. Garvin, J.L. Alvarado, A.M. Jacobi, B.G. Jones, and C.P. Marsh, *Droplet contact angle behavior on a hybrid surface with hydrophobic and hydrophilic properties*. Applied Physics Letters (in review), 2012.

27. Nakamura, M. *Hydrophilic and photocatalytic properties of the SiO<sub>2</sub>/TiO<sub>2</sub> double layers*. in *Proceedings of the Fourth International Symposium on Transparent Oxide Thin Film for Electronics and Optics (TOEO-4)*, April 7, 2005 - April 8, 2005. 2006. Elsevier.
28. Morita, M., T. Koga, H. Otsuka, and A. Takahara, *Macroscopic-wetting anisotropy on the line-patterned surface of fluoroalkylsilane monolayers*. *Langmuir*, 2005. **21**(3): p. 911-918.
29. Choi, W., A. Tuteja, J.M. Mabry, R.E. Cohen, and G.H. McKinley, *A modified Cassie-Baxter relationship to explain contact angle hysteresis and anisotropy on non-wetting textured surfaces*. *Journal of Colloid and Interface Science*, 2009. **339**(1): p. 208-216.
30. Bhushan, B. and Y. Chae Jung, *Wetting study of patterned surfaces for superhydrophobicity*. *Ultramicroscopy*, 2007. **107**(10-11): p. 1033-1041.
31. Extrand, C.W., *Model for contact angles and hysteresis on rough and ultraphobic surfaces*. *Langmuir*, 2002. **18**(21): p. 7991-7999.
32. Drelich, J., J.L. Wilbur, J.D. Miller, and G.M. Whitesides, *Contact angles for liquid drops at a model heterogeneous surface consisting of alternating and parallel hydrophobic/hydrophilic strips*. *Langmuir*, 1996. **12**(7): p. 1913-1922.

33. Carey, V.P., *Liquid-vapor phase-change phenomena: an introduction to the thermophysics of vaporization and condensation processes in heat transfer equipment* 2008: Taylor and Francis.
34. Graham, C. and P. Griffith, *Drop size distributions and heat transfer in dropwise condensation*. International Journal of Heat and Mass Transfer, 1973. **16**(2): p. 337-346.
35. Rose, J.W., *Condensation heat transfer fundamentals*. Chemical Engineering Research and Design, 1998. **76 A2**(A2): p. 143-152.
36. Dietz, C., K. Rykaczewski, A.G. Fedorov, and Y. Joshi, *Visualization of droplet departure on a superhydrophobic surface and implications to heat transfer enhancement during dropwise condensation*. Applied Physics Letters, 2010. **97**(3).